

Parallel Continuum Robots: Modeling, Analysis, and Actuation-Based Force Sensing

Caroline B. Black¹, *Student Member, IEEE*, John Till, *Student Member, IEEE*,
and D. Caleb Rucker¹, *Member, IEEE*

Abstract—Parallel continuum robots (PCRs) combine the compactness, simplicity, and compliance of continuum robots with the precision and strength of rigid-link parallel robots. In this paper, we provide a generalized Cosserat-rod-based kinetostatic model framework that accommodates various joint types and problem formulations (e.g., forward and inverse kinematics under loads, and deflection-based and actuation-based force sensing) useful for simulation and control. Linearization of this general model provides the manipulator Jacobian, end-effector compliance, input stiffness, and wrench reflectivity matrices, which allow us to examine the effect of design parameters on dexterity, force application, and force-sensing ability. Using ellipsoids based on the matrices, we provide a set of design simulations and graphically depict the relationships between pose, actuation, and forces. We further provide a nondimensional analysis of the compliance of PCRs. Finally, we experimentally demonstrate and validate actuation-based force sensing on a prototype six-degree-of-freedom PCR, demonstrating 3-D force sensing with a median magnitude and a directional error of 0.23 N (8% of actual load) and 12°, respectively.

Index Terms—Continuum robots, flexible links, force sensing, parallel robots, robot kinematics.

I. INTRODUCTION

A PARALLEL continuum robot (PCR) is a manipulator with flexible elastic links arranged in parallel. Fig. 1 shows several examples of PCRs with flexible links connected in different configurations, including the traditional six-link Stewart–Gough pattern. The distal ends of the elastic links are connected to the end-effector platform, and the base of each link is independently translated by an actuator at its proximal end. This causes each compliant link to deform, giving rise to articulation of the end effector. This PCR design paradigm achieves multidegree-of-freedom (DOF) articulation and force sensitivity using a structure that is simple, inexpensive,

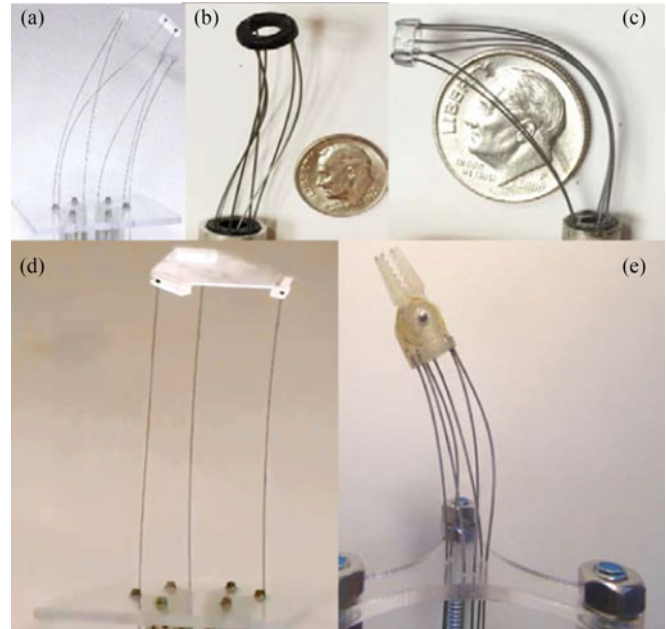


Fig. 1. Parallel continuum design paradigm utilizes the translation of slender rods/tubes between constrained points to create large deformations in each of the flexible links. (a) Stewart–Gough configuration with diameters of 87 mm, (b) 10 mm, and (c) 5 mm. (d) Three-link PCR. (e) Stewart–Gough configuration 12 mm in diameter with a grasper [8].

lightweight, compliant, and easily scalable. These characteristics may be useful in micromanipulation, endoscopic robotic-assisted surgery, and human–robot interaction. This manipulator design category is a natural extension of concepts presented in prior literature on continuum robots and parallel robots [1]–[6], yet its design and potential advantages/tradeoffs have yet to be thoroughly investigated. This paper seeks to further explore the design and analysis achievable with these manipulators and provide insight to application-based design. We also investigate intrinsic force sensing, which uses sensed actuator forces at the base of the manipulator to estimate tip forces.

As detailed in our prior work [7], [8], we believe that this type of design could improve robot-assisted surgical procedures by providing an easily miniaturized remotely actuated manipulator that can achieve multi-DOF articulation in a confined space. Example procedures would include distal vein anastomosis, urethroplasty, ophthalmic surgery, and endoscopic/colonoscopic procedures. Another potential application is to provide a dex-

Manuscript received March 30, 2017; revised July 11, 2017; accepted August 16, 2017. Date of publication December 14, 2017; date of current version February 5, 2018. This paper was recommended for publication by Associate Editor K. Xu and Editor P. Dupont upon evaluation of the reviewers' comments. This work was supported by the National Science Foundation under CMMI-1427122 as part of the NSF/NASA/NIH/USDA/DOD National Robotics Initiative and Graduate Research Fellowship DGE-1452154. Any opinion, findings, and conclusions or recommendations expressed in this material are those of the authors and do not necessarily reflect the views of the National Science Foundation. (Corresponding author: Caroline B. Black.)

The authors are with University of Tennessee, Knoxville, TN 37996 USA (e-mail: cbryson5@vols.utk.edu; JTill@vols.utk.edu; caleb.rucker@utk.edu).

Color versions of one or more of the figures in this paper are available online at <http://ieeexplore.ieee.org>.

Digital Object Identifier 10.1109/TRO.2017.2753829

terous wrist for intra-abdominal surgeries on small structures. PCRs are also potentially applicable to larger scale industrial applications traditionally performed by rigid-link robots to facilitate safer operation around and in cooperation with humans. Because of the inherently lightweight compliant nature of the design, collisions naturally result in deformation to the robot rather than injury to the human. Applications include any cooperative robot task where humans are in direct contact with the robot such as assembly of automotive components and inspection of complex systems [9].

A. Related Work

Current manipulator designs most closely related to the PCR include the multibackbone designs of Simaan *et al.* [3], [10] and the bionic tripod series of manipulators from the German company Festo [11]. Multibackbone designs typically employ serial bending segments along a primary backbone, each of which are actuated by the translation of three secondary backbone rods that terminate at the end of each segment. Within a segment, the rods are constrained by several intermediate spacer disks such that the robot shape can be described by a single backbone curve with piecewise constant curvature. A less constrained parallel continuum structure can be found in [5], [12], and [13], where a miniparallel wrist design employed three short compliant rods connected to the end-effector platform with ball joints. The Festo bionic tripod used the same concept but relaxed the number of intermediate constraints to a single spacer and used four straight actuation rods to achieve three-DOF articulation. Many other continuum robots also employ actuation strategies that can be categorized as parallel across a single manipulator segment with multiple segments concatenated in series (e.g., tendon-driven catheters [14], pneumatic arms [15], [16], and concentric-tube robots [17], [18]).

Kinematic analysis of rigid manipulators has been extensively studied in the past. One objective of this research has been to find adequate performance indices for manipulability and dexterity that would provide a logical option for the optimization of a manipulator's design variables. The most current catalog of these indices is contained in [19]. Most of these measures are related to rigid serial robots. Parallel manipulators have also been investigated in terms of manipulability and accuracy by Merlet [20] and others [21]–[23]. Analyses specifically relating to continuum robots have not been as extensively studied. Workspace analysis for continuum manipulators has been applied to several different systems [24]–[29], and manipulability and force ellipsoids were investigated in [30], which also explored the compliance ellipsoid of continuum manipulators that related the change in a manipulator's position to an external force when the actuators are fixed. Kinesthetic comparisons of different continuum robot designs have also been investigated in [31], where the output stiffness of three different manipulators was measured to compare the different physical designs. One goal of our current work is to provide a general framework for analysis of continuum manipulators in the context of characterizing PCR performance.

Actuation-based force sensing is another topic that is well studied for classical rigid-link manipulators but has not been

widely studied for continuum robots. In conventional rigid-link designs, end-effector wrench is mapped to the joint torques by the transpose of the Jacobian matrix [32] due to conservation of energy. For continuum robots, this simple relationship does not hold true due to the elastic energy stored within the robot links. Gravagne *et al.* showed in [30] that the principle of virtual work can account for the elastic energy storage of a flexible backbone to obtain the true linearized relationship between actuator torques and end-effector forces. When this energy storage is accounted for, accurate actuation-based wrench sensing is possible for multibackbone continuum robots, as has been investigated in [10] and [33]–[35] (termed “intrinsic wrench sensing” in those works). These works derive and validate a wrench-sensing algorithm for constant-curvature manipulators via the principle of virtual work. For the general PCRs used in our research, we use a geometrically exact nonlinear rod-mechanics model to accurately predict the tip force instead of a virtual-work framework under the constant-curvature assumption.

There has also been work in deflection-based force sensing with continuum robots [36] and catheters [37], [38]. However, if a continuum robot is stiff in the axial direction, this approach can become quite ill-conditioned, resulting in high estimation errors. We show that this is also true for PCRs. Our analysis also concludes that the sensitivity to sensing errors is greatly decreased for actuation-based force sensing when compared to deflection-based force sensing.

B. Outline and Contributions

Building on all of the related work discussed above, we first proposed PCRs (of the Stewart–Gough type with no intermediate constraints on the legs) in [39], which provided a kinetostatic model and qualitative analysis of workspace and required actuator forces. In [40], we addressed the computational efficiency of the model implementation, achieving inverse kinetostatics computation speeds in the kilohertz range and demonstrating teleoperation. Then, in [41], we addressed elastic stability of coupled Cosserat rods and developed a computational test for the stability of a model solution. This paper expands and generalizes that same modeling framework without focusing on computational speed or stability, but the computational speeds and stability tests developed in [40] and [41] can easily be realized in the general cases we consider here. In [7] and [8], we experimentally demonstrated the accuracy and dexterity of a 12-mm-diameter, teleoperated, surgical prototype and validated the Cosserat rod model used for solving the robot kinetostatics.

In this paper, we expand and generalize the forward kinetostatics model that was previously presented. This model is more intuitive and unifies the forward kinetostatics with the inverse kinetostatics as well as several other problem formulations that we will identify by only changing the known variables and utilizing the same system of equations. It also accommodates several different types of boundary conditions related to the attachment of the links at the distal platform and to the actuators. In addition to the new model itself, we show how to efficiently linearize the model to obtain the Jacobian, end-effector compliance, input stiffness, and wrench reflectivity matrices. An analysis of these matrices with established metrics

and ellipsoidal visualizations [19] gives rise to several insights regarding the design and capabilities of the manipulator, including force-sensing abilities in different configurations. The matrices are constructed efficiently via a single solution of the boundary value problem (BVP) similar to the approach in [42].

We show that the model framework can solve several problem formulations, three of which can potentially be used to sense forces at the tip of the manipulator. We compare the potential error propagation of these force-sensing methods, including deflection-based force sensing, to arrive at our proposed method of actuation-based force sensing and provide results demonstrating a much lower error sensitivity. Our proposed actuation-based sensing uses actuator positions (6) and actuator forces (6) as inputs and solves the static equilibrium and boundary condition equations for the entire manipulator to calculate both the six-DOF pose and applied end-effector wrench.

This paper is arranged as follows. Section II provides a description of the generalized forward kinetostatics model. Section II provides additional formulations of the kinetostatics model with varying inputs and outputs. The formulation of the linearized kinetostatics matrices is presented in Section III and the resulting analysis of these matrices is also presented. Section IV describes the experimental validation of the sensing kinetostatics model and the force-sensing accuracy of PCRs. Finally, Section V discusses the value of the kinetostatics analysis and future work to be conducted.

II. FORWARD KINETOSTATICS MODEL FRAMEWORK

In this section, we generalize the modeling framework developed in [39] for PCRs and outline the boundary conditions associated with a six-link parallel continuum Stewart–Gough platform. The modeling approach is based on classical Cosserat rod mechanics [43], which have been applied in prior work to develop models for concentric-tube robots [18] and tendon-actuated robots [36]. These equations describe the overall shape and internal forces and moments of a single link. The single-link models are combined to form a PCR model via coupled boundary conditions at the distal and proximal ends of the manipulator, which are then solved simultaneously to obtain the static equilibrium shape of the entire multilink robot. In this paper, we formulate the boundary conditions in a way that unifies the forward and inverse kinetostatics models (and other model formulations which we later identify).

A. Cosserat Rod Equations

A robot consists of n flexible links connected in parallel. The shape of the i th link is defined by its position $\mathbf{p}_i(s_i) \in \mathbb{R}^3$ and material orientation in the form of an orthonormal rotation matrix, $\mathbf{R}_i(s_i) \in \text{SO}(3)$, forming a material-attached reference frame

$$\mathbf{g}_i(s_i) = \begin{bmatrix} \mathbf{R}_i(s_i) & \mathbf{p}_i(s_i) \\ \mathbf{0}^T & 1 \end{bmatrix} \in \text{SE}(3) \quad (1)$$

as a function of arc length $s_i \in [0, l_i]$. Note that $\text{SO}(3)$ and $\text{SE}(3)$ are the special orthogonal and Euclidean groups, as defined in [44]. The position and orientation evolve along the

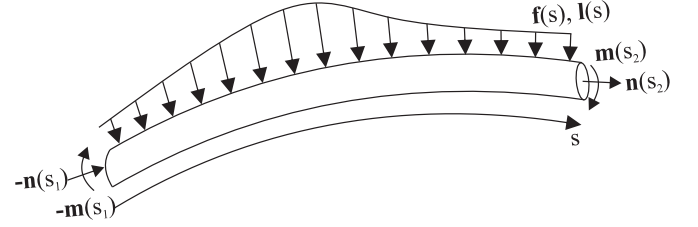


Fig. 2. Arbitrary section of flexible link with the internal force and moment, \mathbf{n} and \mathbf{m} , acting on the portion of the link. The distributed force and moment, $\mathbf{f}(s)$ and $\mathbf{l}(s)$, act along the entire arc length. These forces and moments are written in the global reference frame $\mathbf{g}(s)$.

length of the rod according to the linear, $\mathbf{v}_i(s) \in \mathbb{R}^3$, and angular, $\mathbf{u}_i(s) \in \mathbb{R}^3$, rates of change expressed in local or “body frame” coordinates of the material frame as

$$\begin{aligned} \mathbf{p}'_i &= \mathbf{R}_i \mathbf{v}_i \\ \mathbf{R}'_i &= \mathbf{R}_i \hat{\mathbf{u}}_i \end{aligned} \quad (2)$$

where $'$ denotes a derivative with respect to s_i , and $\hat{\cdot}$ denotes the standard mapping from \mathbb{R}^3 to $\mathfrak{so}(3)$, the Lie algebra of $\text{SO}(3)$, as

$$\hat{\mathbf{u}} = \begin{bmatrix} 0 & -u_3 & u_2 \\ u_3 & 0 & -u_1 \\ -u_2 & u_1 & 0 \end{bmatrix}. \quad (3)$$

As in [44], we also use $^\vee$ to denote the inverse mapping of $\hat{\cdot}$, i.e., $(\hat{\mathbf{u}})^\vee = \mathbf{u}$. The same symbol is overloaded to map \mathbb{R}^6 to $\mathfrak{se}(3)$, the Lie algebra of $\text{SE}(3)$, as

$$\hat{\xi} = \begin{bmatrix} \mathbf{v} \\ \mathbf{u} \end{bmatrix}^\wedge = \begin{bmatrix} 0 & -u_3 & u_2 & v_1 \\ u_3 & 0 & -u_1 & v_2 \\ -u_2 & u_1 & 0 & v_3 \\ 0 & 0 & 0 & 0 \end{bmatrix}. \quad (4)$$

Therefore, if one knows the body-frame \mathbf{v}_i and \mathbf{u}_i vectors and an initial frame $\mathbf{g}_i(0)$, the remaining frames can be obtained by integrating the differential equations in (2), or alternatively, $\dot{\mathbf{g}}_i = \mathbf{g}_i \hat{\xi}_i$. Since \mathbf{v}_i and \mathbf{u}_i are not constant with respect to s_i , numerical integration is required to obtain \mathbf{g}_i .

As derived in [18], [36], and [43], the rates of change of the internal force vector \mathbf{n}_i and internal moment vector \mathbf{m}_i with respect to the arc length s_i are described by the classical Cosserat rod differential equations of static equilibrium. This is done by taking the derivative with respect to arc length of the static equilibrium balance shown in the free body diagram shown in Fig. 2. As derived in [18], this yields

$$\begin{aligned} \mathbf{n}'_i &= -\mathbf{f}_i \\ \mathbf{m}'_i &= -\mathbf{p}'_i \times \mathbf{n}_i - \mathbf{l}_i \end{aligned} \quad (5)$$

where all vectors are expressed in global coordinates, and \mathbf{f}_i and \mathbf{l}_i are distributed force and moment vectors, respectively, applied per unit length to rod i . Distributed self-weight and any other external forces are straightforward to include within \mathbf{f}_i and \mathbf{l}_i (see Fig. 2). For the implementations in this paper, they are negligible and set to zero.

The kinematic variables \mathbf{v}_i and \mathbf{u}_i are related to the material strain (shear, extension, bending, and torsion) and can be used

to calculate the internal force and moment vectors via a material constitutive law. The linear constitutive relationship used follows the form

$$\begin{aligned} \mathbf{n}_i &= \mathbf{R}_i \mathbf{K}_{se,i} (\mathbf{v}_i - \mathbf{v}_i^*), \quad \mathbf{K}_{se,i} = \begin{bmatrix} A_i G_i & 0 & 0 \\ 0 & A_i G_i & 0 \\ 0 & 0 & A_i E_i \end{bmatrix} \\ \mathbf{m}_i &= \mathbf{R}_i \mathbf{K}_{bt,i} (\mathbf{u}_i - \mathbf{u}_i^*), \quad \mathbf{K}_{bt,i} = \begin{bmatrix} E_i I_i & 0 & 0 \\ 0 & E_i I_i & 0 \\ 0 & 0 & J_i G_i \end{bmatrix} \end{aligned} \quad (6)$$

and expresses \mathbf{n}_i and \mathbf{m}_i in global coordinates, where \mathbf{v}_i^* and \mathbf{u}_i^* are the kinematic variables of the rod in an assigned stress-free reference state. For an initially straight rod, the appropriate reference state variables are $\mathbf{v}_i^* = [0 \ 0 \ 1]^T$ and $\mathbf{u}_i^* = [0 \ 0 \ 0]^T$. The matrices $\mathbf{K}_{se,i}$ and $\mathbf{K}_{bt,i}$ contain the stiffness terms for a radially symmetric rod cross section, which could vary with arc length, involving the area A_i , Young's modulus, E_i , shear modulus G_i , second area moment I_i (about the local x - and y -axes), and the polar area moment J_i about the local z -axis.

Thus, for each rod, (2), (5), and (6) form a system of differential equations that describes the evolution of the state variables \mathbf{p}_i , \mathbf{R}_i , \mathbf{n}_i , and \mathbf{m}_i with respect to s_i

$$\begin{aligned} \mathbf{p}_i' &= \mathbf{R}_i \mathbf{v}_i, \quad \mathbf{v}_i = \mathbf{K}_{se,i}^{-1} \mathbf{R}_i^T \mathbf{n}_i + \mathbf{v}_i^* \\ \mathbf{R}_i' &= \mathbf{R}_i \hat{\mathbf{u}}_i, \quad \mathbf{u}_i = \mathbf{K}_{bt,i}^{-1} \mathbf{R}_i^T \mathbf{m}_i + \mathbf{u}_i^* \\ \mathbf{n}_i' &= -\mathbf{f}_i \\ \mathbf{m}_i' &= -\mathbf{p}_i' \times \mathbf{n}_i - \mathbf{l}_i. \end{aligned} \quad (7)$$

The force and moment equations are also sometimes expressed in body-frame coordinates. The above equations describe the shape and the internal forces and moments of the i th link. In the next section, we detail how the design of the distal end effector and the proximal base platform create geometric constraints. These constraints are enforced along with end-effector static equilibrium via a coupled set of boundary conditions that are simultaneously solved to obtain the configuration of the manipulator.

B. Distal Boundary Conditions

Regardless of the joint type connecting the flexible links to the end-effector platform, the following conditions of static equilibrium are enforced for the end effector by summing forces and moments about the global origin:

$$\begin{aligned} \sum_{i=1}^n [\mathbf{n}_i(l_i)] - \mathbf{F} &= \mathbf{0} \\ \sum_{i=1}^n [\mathbf{p}_i(l_i) \times \mathbf{n}_i(l_i) + \mathbf{m}_i(l_i)] - \mathbf{p}_e \times \mathbf{F} - \mathbf{M} &= \mathbf{0} \end{aligned} \quad (8)$$

where \mathbf{F} and \mathbf{M} are external force and moment vectors, expressed in global coordinates and applied at the centroid of the end effector, \mathbf{p}_e . We combine the applied loads into a “wrench” vector $\mathbf{w} = [\mathbf{F}^T \ \mathbf{M}^T]^T$ for notational compactness. Also, the position of the distal end of the link is related to the center

TABLE I
DISTAL BOUNDARY CONDITIONS FOR JOINT TYPES

Joint Type	Specified at $s_i = l_i$
Fixed	Equation (8)
	Equation (9)
	Equation (12)
Torsionless	Equation (8)
	Equation (9)
	$\mathbf{e}_3^T \mathbf{R}_i^T \mathbf{m}_i(l_i) = 0, i = 1, \dots, n$ $(\log(\mathbf{R}_i^T(l_i) \mathbf{R}_e \mathbf{R}_{\alpha_i}))^\vee _{xy} = \mathbf{0}, i = 1, \dots, n$
Spherical	Equation (8)
	Equation (9)
	$\mathbf{R}_e^T \mathbf{m}_i(l_i) = \mathbf{0}, i = 1, \dots, n$

of the end effector via a constant vector \mathbf{p}_i expressed in the end-effector frame

$$\mathbf{p}_e + \mathbf{R}_e \mathbf{p}_i - \mathbf{p}_i = \mathbf{0}, \quad i = 1, \dots, n. \quad (9)$$

The remaining distal boundary conditions govern the material orientation and moment of the links at $s_i = l_i$ based on the joint types, which connect them to the end-effector platform. We explain these rotation conditions below and summarize the entire set distal boundary conditions for each joint type in Table I.

1) *Fixed Joints*: In the case of fixed joints (Table I “Fixed”), the orientation of the end-effector platform frame, \mathbf{R}_e , and the orientation of each link at the tip, $\mathbf{R}_i(l_i)$, are related by a pre-defined offset orientation, \mathbf{R}_{α_i} (dependent on the distal platform design). This constant rotation between end-effector and link end frames and the link frame is

$$\mathbf{R}_{\alpha_i} = \mathbf{R}_e^T \mathbf{R}_i(l_i), \quad i = 1, \dots, n \quad (10)$$

where the matrix \mathbf{R}_{α_i} is defined by $\alpha_i \in \mathbb{R}^3$, the angular displacement vector with respect to the global frame. This rotation can be constructed via matrix exponential and the mapping in (3)

$$\mathbf{R}_{\alpha_i} = e^{\hat{\alpha}_i}, \quad i = 1, \dots, n. \quad (11)$$

To eliminate redundant equations and facilitate a numerical solution, the angular relationship can be written in the reduced form

$$[\log(\mathbf{R}_i(l_i)^T \mathbf{R}_e \mathbf{R}_{\alpha_i})]^\vee = \mathbf{0}, \quad i = 1, \dots, n \quad (12)$$

where $\log()$ is the matrix natural logarithm, which maps $\text{SO}(3)$ to $\mathfrak{so}(3)$ and the $^\vee$ operator subsequently maps $\mathfrak{so}(3)$ to \mathbb{R}^3 . This form was chosen to express the angular error in the local $\mathbf{R}_i(l_i)$ frame, which facilitates a unified presentation of the torsionless case we discuss below. In the prototype used in our experiments, $\alpha_i = \mathbf{0}$, so the orientation of each link must equal the orientation of the end effector.

2) *Torsionless Joints*: If the links are connected to the end-effector with rotary joints allowing axial rotation, only the tangent vector of the link is fixed at $s_i = l_i$, and the link's rotation about its tangent vector is initially unknown and must be found. This implies the “natural boundary condition” that the z (torsional) component of the body frame moment, i.e., $\mathbf{e}_3^T \mathbf{R}_i^T \mathbf{m}_i(l_i)$

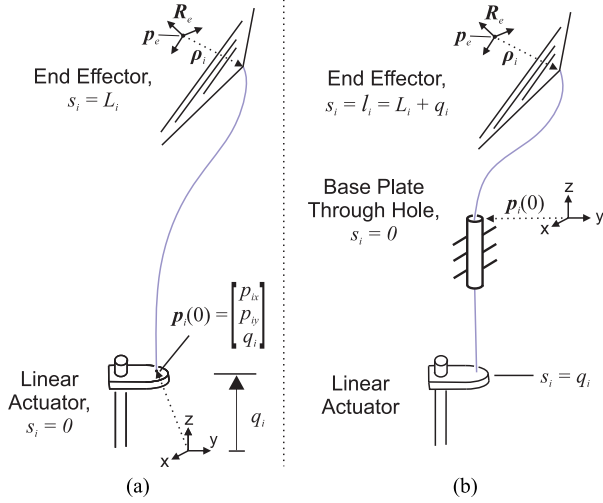


Fig. 3. Manipulator variables without and with a base plate in (a) and (b), respectively. The differences arise in the length of integration of the link and the definition of the arc length datum $s_i = 0$ for each link. The linear actuator controls the q_i , which is equal to the initial position $p_z(0)$ of the link in the global frame. When a base plate is included, the linear actuator effectively changes the arc length l_i beyond the base plate. Without the base plate, the link arc length is constant, but the initial position of the link is changed. The constant offset vector \mathbf{p}_i which defines the distal connection point is shown in the end-effector frame.

($\mathbf{e}_3 = [0 \ 0 \ 1]$) must be zero. Therefore, only the x and y components of the distal constraints on the link rotation matrix in (12) should be applied. This is designated with the $[\cdot]_{x,y}$ in Table I and is equivalent to multiplying by a truncated identity matrix, which eliminates the third row. We note that if there are no distributed moments along the links and the links are straight in their unstressed reference states, a torsionless joint at the tip implies zero torsion everywhere along the link as a consequence of the differential equations defining the rod shape [see (7)]. In this paper, torsionless joints are used for the simulations and experiments performed with the physical robot.

3) *Spherical Joints*: Having a spherical joint at the tip of each link implies the natural boundary condition of zero moment at the tip of each link, $\mathbf{R}_i^T \mathbf{m}(l_i) = \mathbf{0}$. The distal orientation of the links is now unknown and must be found.

C. Proximal Boundary Conditions

We formulate proximal boundary conditions for two possible types of robot base designs illustrated in Fig. 3: 1) robots with links passing through holes in a base plate between the actuators and the distal platform (Base Plate design); and 2) robots with links that are connected directly to the actuators and unconstrained along their full length (No Base Plate design). The inclusion of different base plate configurations is provided for generality of the modeling. A design with no base plate eliminates a source of friction and is thus more conducive to force sensing. It also raises the possibility of augmenting the actuation space to include general six-DOF motion of the rod bases in addition to pure axial translation, as envisioned and explored recently in [45] and [46]. A base plate design provides greater stability for distal devices and would be appropriate for endoscopic

TABLE II
PROXIMAL BOUNDARY CONDITIONS

Configuration	Joint Type	Specified at $s_i = 0$	Unknown
No Base Plate	Fixed	$\mathbf{p}_i = [p_{ix}, p_{iy}, q_i]^T$ $\mathbf{R}_i = \mathbf{R}_z(\phi_i)$	\mathbf{n}_i \mathbf{m}_i
No Base Plate	Torsionless	$\mathbf{p}_i = [p_{ix}, p_{iy}, q_i]^T$ $m_{iz} = 0$ $\mathbf{R}_i = \mathbf{R}_z(\phi_i)$	\mathbf{n}_i m_{ix}, m_{iy} ϕ_i
No Base Plate	Spherical	$\mathbf{p}_i = [p_{ix}, p_{iy}, q_i]^T$ $\mathbf{m}_i = \mathbf{0}$ $\mathbf{R}_i = \mathbf{R}_i(\theta_i)$	\mathbf{n}_i θ_i
Base Plate	Fixed	\mathbf{p}_i $\mathbf{R}_i = \mathbf{R}_z(\theta_i)$	\mathbf{n}_i \mathbf{m}_i
Base Plate	Torsionless	\mathbf{p}_i $m_{iz} = 0$ $\mathbf{R}_i = \mathbf{R}_z(\phi_i)$	\mathbf{n}_i m_{ix}, y ϕ_i

applications where the parallel structure manipulates flexible tools passing through an inner lumen [see Fig. 1(b) and (c)]. We also consider three proximal joint types (fixed, torsionless, and spherical). This extends our prior work, where we considered designs with base plates and torsionless proximal joints.

Our solution procedure (detailed in the next section) requires known conditions to be specified at a reference point on each link $s_i = 0$ and any unknown variables to be guessed. Table II details the specified and unknown proximal variables for the relevant joint types and base plate configurations. We note that the specified variables are functions of the actuator displacement q_i , fixed design parameters p_{ix} and p_{iy} , and some of the unknown variables at $s_i = 0$ as we describe in detail below. In both the base-plate and no-base-plate configurations (see Fig. 3), the actuation variable, q_i , is defined as the z -axis position of the base of the link in some fixed global reference frame.

1) *No Base Plate Present*: Without a base plate, $s_i = 0$ is designated, where the link attaches to the actuator, and the length of integration is the entire length of the link, $l_i = L_i$. The position at $s_i = 0$ is specified by \mathbf{p}_i , which contains the actuation variable q_i as the global z position of each proximal link end, as shown in Fig. 3(a).

When connections are fixed, the base rotation of each link $\mathbf{R}_i(0)$ is a function of ϕ_i , a specified rotation about the z -axis, which could be a constant parameter or controlled as an additional input DOF if rotational actuators were employed. The internal force and moment at $s_i = 0$ are guessed variables.

For torsionless connections, $m_{iz}(0) = 0$, and the initial rotation is a function of an unknown rotation ϕ_i about the z -axis. The internal force and the x and y components of \mathbf{m}_i at $s_i = 0$ are guessed.

In the case of spherical joints, $\mathbf{m}_i(0) = \mathbf{0}$ and the link has an unknown initial orientation, $\mathbf{R}_i(0)$, which can be parameterized by $\theta_i(0) \in \mathbb{R}^3$, a vector of three angular displacements as

$$\mathbf{R}_i(0) = e^{\hat{\theta}_i}. \quad (13)$$

These rotations are guessed and used to construct $\mathbf{R}_i(0)$. The internal force at $s_i = 0$ is guessed.

2) *Base Plate Present*: With a base plate, we assume that the portion of the link between the actuator and the base plate is always straight. This is true as long as:

- 1) this portion of the link is not precurved;
- 2) the tangent vector of the hole in the base plate is designed to pass through the actuator connection point;
- 3) the axial compressive load is lower than the Euler critical buckling load for the current length of unsupported rod.

We designate $s_i = 0$ at the base platform and integrate the differential equations from there to $s_i = l_i$, the length of the link between the base plate and the distal platform, which is a function of q_i , as

$$l_i = L_i + q_i. \quad (14)$$

As shown in Fig. 3, we have defined the global reference frame such that its xy plane is coplanar with the base platform, and thus, each q_i is negative. With a base plate present and fixed joints, torsional deformation of each link between the actuator and the base plate should be considered. In this straight section, the Cosserat equations imply that the angular rate of change in the axial direction, $u_{iz} = \frac{m_{iz}}{J_i G_i}$, is constant. Therefore, the angle of axial rotation, $\theta_{i,z}(s_i)$, varies linearly with arc length in this section. Under these assumptions, the initial condition $\theta_{i,z}(0)$ is a linear function of the actuation variable q_i , and the unknown torsional moment, m_{iz} , at $s_i = 0$ as

$$\theta_{i,z}(0) = \phi_i - q_i \frac{m_{iz}(0)}{J_i G_i}. \quad (15)$$

where ϕ_i is the initial axial rotation of the link at the point of attachment. The initial z -axis rotation matrix for the link is then a function of $\theta_{i,z}$,

$$\mathbf{R}_i(0) = \mathbf{R}_z(\theta_{i,z}) = e^{\theta_{i,z} \hat{\mathbf{e}}_3} \quad (16)$$

where $\mathbf{e}_3 = [0 \ 0 \ 1]^T$. In the case of fixed connections to the actuators, the proximal position of the links is specified with the vector $\mathbf{p}_i = [p_{ix} \ p_{iy} \ 0]^T$ and the internal force and moment are guessed. For torsionless connections at the actuators, $m_{iz}(0) = 0$ and $\mathbf{R}_i(0)$ is only a function of ϕ_i , which is a guessed variable along with the internal force and the x and y components of the internal moment.

D. Solution Method for Forward Kinematics

To lay groundwork for discussing the generalized problem formulations in the next subsection, we here detail our numerical solution procedure for the forward kinetostatics BVP. The differential equations for the i th link [see (7)] have the form

$$\mathbf{y}'_i = \mathbf{f}(\mathbf{y}_i, s_i) \quad (17)$$

where $\mathbf{y}_i = \{\mathbf{g}_i, \mathbf{n}_i, \mathbf{m}_i\}$ (see (1) for definition of \mathbf{g}_i).

At the proximal end of the link ($s_i = 0$), the elements of each \mathbf{y}_i are specified as functions of known or unknown proximal variables (see Table II). At the distal end of the robot ($s_i = l_i$), the boundary conditions consist of six joint-specific geometric constraints for each distal link end (given in Table I), and six static equilibrium equations for the entire end effector [given by (8)], which involves the distal variables of all the rods. Thus, this

set of $6n + 6$ distal boundary conditions effectively couple the individual rod models (7) together, and the entire coupled system must be solved simultaneously. We solve the coupled system via a shooting method, which iteratively guesses the entire set of unknowns, integrates all rod initial value problems (7), and evaluates the entire set of coupled boundary conditions. The guess is updated based on the results of the boundary residual calculation until the set tolerance is satisfied. We describe the organization of this process in detail below for the forward kinetostatics problem and adapt the same approach to solve the generalized problem formulations in the next section. The general process is depicted by an algorithmic flowchart in Fig. 4.

In order to solve the coupled system, we can vertically concatenate all of the distal boundary equations (given by the equations listed in Table I according to joint type) into a single vector equation

$$\mathbf{b}(\mathbf{g}_e, \mathbf{q}, \mathbf{w}, \boldsymbol{\tau}, \boldsymbol{\gamma}) = \mathbf{0} \quad (18)$$

where $\mathbf{q} = [q_1 \dots q_n]$ contains the actuator variables, $\mathbf{w} = [\mathbf{F}^T \ \mathbf{M}^T]^T$ is the external tip wrench, $\boldsymbol{\tau} = [-n_{i,z}(0) \dots -n_{n,z}(0)]^T$ contains the actuator forces, all remaining unknown proximal variables are contained in $\boldsymbol{\gamma}$, and \mathbf{g}_e is the (unknown) pose of the end effector

$$\mathbf{g}_e = \begin{bmatrix} e^{\hat{\boldsymbol{\varphi}}} & \mathbf{p}_e \\ \mathbf{0} & \mathbf{I} \end{bmatrix} \quad (19)$$

with $\boldsymbol{\varphi} = [\varphi_x \ \varphi_y \ \varphi_z]^T$ and $\mathbf{p}_e = [p_{ex} \ p_{ey} \ p_{ez}]^T$. For example, in the case of proximal and distal fixed joints, (18) contains (8), (9), and (12), and with a base plate, $\boldsymbol{\gamma} = [n_{1,x}(0) \ n_{1,y}(0) \ \mathbf{m}_1^T(0) \dots n_{n,x}(0) \ n_{n,y}(0) \ \mathbf{m}_n^T(0)]^T$.

Note that while \mathbf{q} , $\boldsymbol{\tau}$, and $\boldsymbol{\gamma}$ do not explicitly appear in Table I, \mathbf{b} is implicitly dependent on them through the distal link variables. For any given guess of $\boldsymbol{\tau}$, $\boldsymbol{\gamma}$, and \mathbf{g}_e and specification of \mathbf{q} and \mathbf{w} , we can integrate the differential equations for each link from base to tip and subsequently evaluate the function $\mathbf{b}(\mathbf{g}_e, \mathbf{q}, \mathbf{w}, \boldsymbol{\tau}, \boldsymbol{\gamma})$, which we call the boundary condition residual. In prior work [39], we formulated the forward kinetostatics residual in a minimal way with only $6n$ equations that did not contain the unknown \mathbf{g}_e . By here introducing \mathbf{g}_e as an extra six-DOF unknown, the distal geometric constraints are written more intuitively in terms of \mathbf{R}_e and \mathbf{p}_e in Table I. This new approach also unifies the generalized problem formulations in the next section by identifying a common set of equations that they all must solve. Note that in this form of the forward kinetostatics problem, (18) contains $6n + 6$ scalar equations, and the number of unknowns is also $6n + 6$, with $\boldsymbol{\gamma}$ containing $5n$ unknowns, $\boldsymbol{\tau}$ containing n unknowns, and \mathbf{g}_e containing three positions and three rotational DOFs as unknowns.

We use a shooting method to solve the system of equations in Table I for the specific manipulator design being modeled. The unknown proximal boundary conditions ($\boldsymbol{\gamma}$), the actuator forces ($\boldsymbol{\tau}$), and the end-effector pose (\mathbf{g}_e) are guessed. These guessed values along with the specified values are used to numerically integrate the differential equations from $s_i = 0$ to l_i as an initial value problem (we use the `ode45` solver, which implements the Dormand–Prince method), and the distal boundary condition

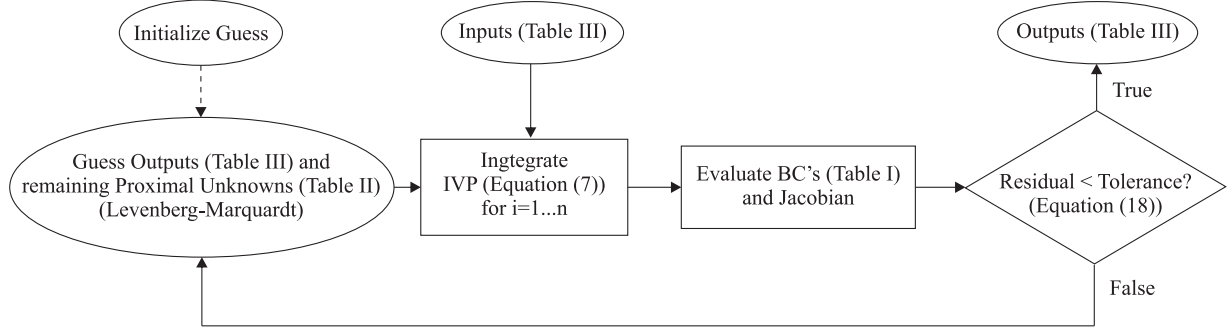


Fig. 4. Our shooting method for solving any general problem formulation. The input variables are specified, and the unknown and output variables are guessed.

equations are subsequently evaluated. This process is nested within an outer nonlinear-solver loop, which iteratively updates the guessed values until the distal boundary conditions are satisfied within an appropriate tolerance. To update the guesses, we have used MATLAB's `fsolve()` function. This solver can be configured to implement several of algorithms; in this case, we used the trust-region dogleg algorithm. We examine the rotation matrix solution to verify that it stays close to orthonormal, but we do not explicitly enforce orthonormality. Orthonormality is usually preserved quite well due to the high-order numerical integration methods, the short integration length, and low curvatures of the flexible links.

In [40], we described how this shooting method can be efficiently implemented in C++ to solve the inverse kinematics problem at rates greater than 4 kHz, thus enabling online control. This paper focuses on offline tasks, so runtime performance is a minor consideration when selecting a programming language. In the studies performed in this paper, we chose MATLAB for its high-level language benefits of readability and a dynamic runtime environment.

E. Generalized Problem Formulations

Equation (18) represents boundary conditions that must always be satisfied. Since \mathbf{b} is written as a multivariable function of \mathbf{g}_e , \mathbf{q} , \mathbf{w} , $\boldsymbol{\tau}$, and $\boldsymbol{\gamma}$, the outer nonlinear solver loop outlined in the previous section can be easily adapted to solve other general problem formulations (beyond forward kinetostatics) by merely assigning appropriate sets of known and unknown (iteratively guessed) variables. For example, if we want to know the \mathbf{q} and $\boldsymbol{\tau}$ required to achieve a specified \mathbf{g}_e under a known constant load \mathbf{w} (which could be considered an inverse kinetostatics problem), the integration procedure remains the same, but the nonlinear solver must iteratively guess the unknowns \mathbf{q} and $\boldsymbol{\tau}$ and evaluate \mathbf{b} with the specified \mathbf{g}_e and \mathbf{w} . In general, any combination of variables out of the set $\{\mathbf{g}_e, \mathbf{q}, \mathbf{w}, \boldsymbol{\tau}\}$ can be selected as knowns with the remaining variables as unknowns, as long as the number of unknowns matches the number of equations in \mathbf{b} . Fig. 4 summarizes the process in general, and we describe several useful cases below.

Table III shows several possible kinetostatic problem formulations and their inputs and outputs (knowns and unknowns) along with their respective number of unknowns, which can be

TABLE III
KINETOSTATIC MODEL FORMULATIONS

Formulation	Number of Unknowns	Number of Equations
$\{\mathbf{g}_e, \boldsymbol{\tau}\} = \mathbf{F}_{q,w}(\mathbf{q}, \mathbf{w})$	$6n + 6$	$6n + 6$
$\{\mathbf{g}_e, \mathbf{q}\} = \mathbf{F}_{\tau,w}(\boldsymbol{\tau}, \mathbf{w})$	$6n + 6$	
$\{\mathbf{q}, \boldsymbol{\tau}\} = \mathbf{F}_{g,w}(\mathbf{g}_e, \mathbf{w})$	$7n$	
$\{\boldsymbol{\tau}, \mathbf{w}\} = \mathbf{F}_{g,q}(\mathbf{g}_e, \mathbf{q})$	$6n + 6$	
$\{\mathbf{q}, \mathbf{w}\} = \mathbf{F}_{g,\tau}(\mathbf{g}_e, \boldsymbol{\tau})$	$6n + 6$	
$\{\mathbf{g}_e, \mathbf{w}\} = \mathbf{F}_{q,\tau}(\mathbf{q}, \boldsymbol{\tau})$	$5n + 12$	

compared to the number of equations which is a constant $6n + 6$. The first two formulations are forward kinetostatics variants, based on either known actuator displacements or forces. We briefly discussed the inverse kinetostatics problem formulation above, and this is labeled $\mathbf{F}_{g,w}$ in the table. The last three problem formulations in the table contain the external wrench as an output. Thus, these formulations represent different ways to calculate the wrench at the tip of the manipulator, given various known or sensed quantities. The formulation using inputs of \mathbf{g}_e and \mathbf{q} is essentially the deflection-based wrench sensing explored using a probabilistic framework in [36]. The $\mathbf{F}_{g,\tau}$ formulation is also a deflection-based sensing formulation, since it has \mathbf{g}_e as an input. $\mathbf{F}_{q,\tau}$ is not based on deflection and is perhaps the most convenient wrench sensing formulation, since the actuation variables and forces are easily accessible through sensors mounted at the actuators themselves.

We call the $\mathbf{F}_{q,\tau}$ formulation “actuation-based wrench sensing.” This idea has been previously termed “intrinsic wrench sensing” in [33], which used a constant-curvature model framework in contrast to our general Cosserat rod approach in Section II. We evaluate our approach experimentally for PCR's in Section IV, and we analytically show that for our prototype PCR design, actuation-based sensing is less sensitive to measurement errors than either deflection-based approach.

We note that the $\mathbf{F}_{g,w}$ formulation (inverse kinetostatics) is underconstrained for $n > 6$ (which can be addressed by incorporating some method for redundancy resolution) and overconstrained for $n < 6$ (which can be resolved by reducing in the dimension of the pose specification). For example, we should consider the number of desired operational DOFs versus the number of actuator inputs (n). If a six-DOF robot is used for

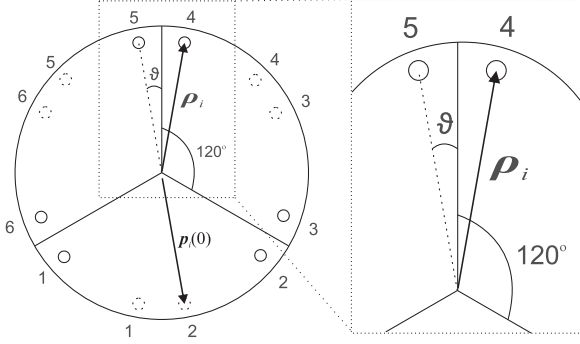


Fig. 5. Top view of a manipulator in the nominal straight configuration. The base origins of links one through six are denoted by the numbered dashed circles. The distal connection points of links one through six are denoted by the numbered solid circles. The angular offset of point pairs from the 120° lines of symmetry is shown here as 10° . This offset can be increased or decreased by changing the location of the holes in the end-effector platform and the base, and this will change the behavior of the manipulator. \mathbf{p}_i is the constant offset vector from the center of the distal platform to the distal end of link i , expressed in the end-effector frame.

only position control, the $F_{g,w}$, $F_{g,q}$, and $F_{g,\tau}$ algorithms will be underdetermined, and a method for redundancy resolution should be incorporated. Similarly, the actuation-based sensing formulation is overconstrained if $n > 6$ (which could be resolved by a least-squares solution or a probabilistic approach) and underconstrained for $n < 6$ (which could be resolved by reducing the dimension of sensed wrench components, e.g., assuming some components are zero).

F. Specific Modeling Example

The particular robot design analyzed in the next section is a Stewart–Gough design with a base plate. At the base, the link origin points are offset from the three 120° dividing lines by $\vartheta = 10^\circ$ and occur at a radius of 87 mm (see dashed circles in Fig. 5). This geometry defines \mathbf{p}_i (the global origin is the center of the base plate). At the distal end, the link connection points are also offset from three 120° dividing lines by $\vartheta = 10^\circ$ at the same radius, but the pattern is shifted by 60° and the link pair numbering is shifted by one (see solid circles in Fig. 5). For example, links 1 and 2 are paired at the base, but 2 and 3 are paired at the tip. This geometry defines \mathbf{p}_i . The distal and proximal boundary conditions are torsionless (see Tables I and II). We assume there are no distributed loads on the individual links ($\mathbf{f}_i = 0$ and $\mathbf{l}_i = 0$), but we could easily specify them if needed. We can solve the $F_{q,w}$ model formulation by specifying actuator displacements and the external wrench (nominally $\mathbf{F} = 0$ and $\mathbf{M} = 0$) and including the end-effector pose and actuation forces in the vector of unknowns that is obtained via the shooting method. Alternatively, we could specify any other pair of quantities and solve for the remaining pair according to the formulations (see Table III). The equations solved are exactly the same. The only difference is which variables are specified and which are included in the set of unknowns. The solution in the nominal case where all leg lengths are $l_i = 400$ mm is $\mathbf{p}_e = [0 \ 0 \ 396]^T$ mm and $\mathbf{R}_e = \mathbf{I}$. This design is similar to the

prototype presented in our previous work [39]. The design we consider in Section IV has different physical parameters, which are more conducive to the force-sensing experiments. A six-link platform design was used to take advantage of the square system of inputs and outputs in order to analyze the position and rotation Jacobian matrices alongside the compliance and force reflectivity matrices. The choice of a Stewart–Gough-like hexapod arrangement for the legs provides well-conditioned control of six-DOF pose and wrench sensing.

III. KINETOSTATIC ANALYSIS

In this section, we identify four kinetostatic matrices that represent the linearized robot behavior near a particular solution of the kinetostatics model. We show how to numerically compute these matrices with minimal computational overhead beyond what is already required to solve the kinetostatics BVP. We then analyze the design of PCRs with these matrices via matrix ellipsoids, matrix metrics, nondimensional analysis, and force application calculations. We specifically examine four representative poses and three representative designs.

A. Model Linearization

Linearizing the $F_{q,w}$ formulation about the current robot configuration produces the following two equations:

$$\begin{aligned} (\mathbf{g}_e^{-1} \delta \mathbf{g}_e)^\vee &= \mathbf{J} \delta \mathbf{q} + \mathbf{C} \delta \mathbf{w} \\ \delta \boldsymbol{\tau} &= \mathbf{K} \delta \mathbf{q} + \mathbf{W} \delta \mathbf{w} \end{aligned} \quad (20)$$

where δ denotes a very small change. In the first equation, we recognize the conventional definition of the $6 \times n$ body-frame Jacobian, \mathbf{J} (mapping changes in joint positions to the corresponding changes in end-effector pose expressed in body-frame coordinates) and 6×6 body-frame compliance matrix, \mathbf{C} , (mapping changes in global applied wrench to body-frame pose change). This relationship has been stated for continuum robots in [30] and [42] and is also generally true for robots with series-elastic actuators [47], [48] due to the flexible link between the applied actuator force and the load. In the second equation, the $n \times n$ matrix, \mathbf{K} (which we henceforth refer to as the “input stiffness”), maps changes in joint positions to changes in actuator forces, and the $n \times 6$ matrix, \mathbf{W} (which we call the “wrench reflectivity matrix”), maps changes in applied wrench to changes in actuator loads. As mentioned in the introduction, for rigid-link robots, $\mathbf{C} = \mathbf{0}$, $\mathbf{K} = \mathbf{0}$, and $\mathbf{W} = \mathbf{J}^T$ [32]. The last result is typically derived by equating power input at the actuators to the power output at the end effector, which implicitly assumes that the robot itself does not store energy during loading. Thus, $\mathbf{W} \neq \mathbf{J}^T$ for continuum robots because the elastic energy stored within the robot itself can change when loads are applied.

B. Efficient Computation of Kinetostatics Matrices

In order to analyze and design the kinetostatics characteristics of a flexible manipulator, it is important to efficiently compute the required kinetostatic matrices described above. We now show that \mathbf{J} , \mathbf{C} , \mathbf{K} , and \mathbf{W} can be calculated with min-

imal computational effort after solving the general BVP that defines any of the problem formulations outlined in Table III. This method is similar to the one proposed in [42]. Equation (18) can be linearized about the current configuration in terms of pose (\mathbf{g}_e), actuator variables (\mathbf{q}), actuator forces ($\boldsymbol{\tau}$), and external wrench (\mathbf{w}), and the vector of remaining proximal unknowns $\boldsymbol{\gamma}$. Any small change in the residual function then has the form

$$\delta \mathbf{b} = \mathbf{B}_\tau \delta \boldsymbol{\tau} + \mathbf{B}_q \delta \mathbf{q} + \mathbf{B}_w \delta \mathbf{w} + \mathbf{B}_g (\mathbf{g}_e^{-1} \delta \mathbf{g}_e)^\vee + \mathbf{B}_\gamma \delta \boldsymbol{\gamma}. \quad (21)$$

The \mathbf{B} matrices in the above equation can be numerically approximated by the following finite-difference procedure. For $\mathbf{B}_\tau, \mathbf{B}_q, \mathbf{B}_w, \mathbf{B}_\gamma$:

- 1) Increment an element of either $\boldsymbol{\tau}$, \mathbf{q} , \mathbf{w} , or $\boldsymbol{\gamma}$ by a small amount Δ from its nominal value (which is either known or has already been obtained in the solution of the BVP). If the incremented variable is an element of \mathbf{w} , go directly to step 3.
- 2) Solve (17) for the link that is associated with the incremented variable from base to tip as an initial value problem.
- 3) Evaluate the change in \mathbf{b} that the increment produced and divide by Δ . The resulting vector is assigned in the appropriate column of the \mathbf{B} matrix associated with the incremented variable.

For \mathbf{B}_g :

- 1) Increment \mathbf{g}_e as

$$\Delta \mathbf{g}_e = \mathbf{g}_{e,i} \hat{\mathbf{e}}_i \Delta \quad (22)$$

where $\hat{\cdot}$ maps \mathbb{R}^6 to $\mathfrak{se}(3)$ as given in (4), and \mathbf{e}_i is a column vector of zeros with 1 in the i th row.

- 2) Evaluate the change in \mathbf{b} that the increment produced and divide by Δ . The resulting vector is assigned in the i th column of the \mathbf{B}_g matrix.

Note that \mathbf{B}_g and \mathbf{B}_w could also be obtained analytically by direct differentiation of \mathbf{b} , since \mathbf{w} and \mathbf{g}_e appear explicitly in the distal boundary condition equations.

After solving the BVP and obtaining all of the \mathbf{B} matrices, we can obtain the four kinetostatic matrices by observing that the residual vector, \mathbf{b} , must remain equal to zero for any small change in any variable during robot operation (the BVP must be satisfied at all times). Thus, setting $\delta \mathbf{b} = 0$ and rearranging provides

$$\begin{bmatrix} \delta \boldsymbol{\gamma} \\ (\mathbf{g}_e^{-1} \delta \mathbf{g}_e)^\vee \\ \delta \boldsymbol{\tau} \end{bmatrix} = \mathbf{G} \begin{bmatrix} \delta \mathbf{q} \\ \delta \mathbf{w} \end{bmatrix} \quad (23)$$

where

$$\mathbf{G} = -[\mathbf{B}_\gamma \mid \mathbf{B}_g \mid \mathbf{B}_\tau]^{-1} [\mathbf{B}_q \mid \mathbf{B}_w] \quad (24)$$

and the matrix inverted above is square of dimension $6n + 6$. \mathbf{G} then contains the four kinetostatic matrices as appropriately

TABLE IV
MATRIX INDICES

Pose	μ			
	\mathbf{J}_p	\mathbf{J}_r	\mathbf{C}_f	\mathbf{W}_f
Nominal	4.93	0.27	9.25E-12	0.25
Equal Aspect Ratio	0.34	0.13	4.45E-16	15.25
Angular Offset (+10°)	16.52	0.45	2.11E-12	0.06
Twisting	2.85	0.01	5.93E-07	65.62
Translating	3.64	0.22	6.06E-10	0.46
Bending	1.30	0.12	1.86E-07	7.40

Pose	β			
	\mathbf{J}_p	\mathbf{J}_r	\mathbf{C}_f	\mathbf{W}_f
Nominal	0.36	0.44	0.09	0.19
Equal Aspect Ratio	0.99	0.87	0.97	0.99
Angular Offset (+10°)	0.24	0.19	0.04	0.08
Twisting	0.60	0.21	0.06	0.82
Translating	0.38	0.50	0.026	0.25
Bending	0.56	0.61	0.10	0.81

dimensioned subblocks, which can be extracted from it

$$\mathbf{G} = \begin{bmatrix} \boldsymbol{\Gamma} \\ \mathbf{J}_{6 \times n} & \mathbf{C}_{6 \times 6} \\ \mathbf{K}_{n \times n} & \mathbf{W}_{n \times 6} \end{bmatrix} \quad (25)$$

where $\boldsymbol{\Gamma}$ is the matrix relating the actuation variables and the tip wrench to $\boldsymbol{\gamma}$.

C. Matrix Analysis

In this section, we employ several matrix metrics (see Table IV) and visualize aspects of an example robot's behavior (physical parameters are provided in Section II-F) with ellipsoids (see Figs. 6 and 7). The goal will be to characterize the robot's abilities in terms of manipulability, force application, stiffness, and force sensing using the \mathbf{J} , \mathbf{C} , \mathbf{K} , and \mathbf{W} matrices. While the use of the Jacobian and compliance matrices is well known, the stiffness matrix will aid in motor selection for specific designs by estimating the forces required to actuate the flexible links. Finally, the wrench reflectivity matrix can be used to estimate the robot's ability to intrinsically sense applied tip wrenches via the measurement of the actuator loads.

The Jacobian is commonly used to measure manipulability by analyzing several different metrics, including the determinant, the condition number of the matrix, and the volume of ellipsoids drawn from either the singular values or the eigenvalues and eigenvectors of the matrix [19], [20], [32]. In order to avoid the mixture of rotational and positional units, we have calculated separate ellipsoids for position and rotation manipulability (see Figs. 6 and 7, rows 1 and 2). It is also possible to assign a characteristic length in order to appropriately scale the rotational elements and then analyze the entire matrix. However, this choice is arbitrary and difficult to visualize in 2D.

We generate a manipulability ellipsoid for the position and rotation portions of the matrix by mapping a unit sphere in joint space to an ellipsoid in end-effector Cartesian space by transforming it with the Jacobian. Then, the magnitude of the

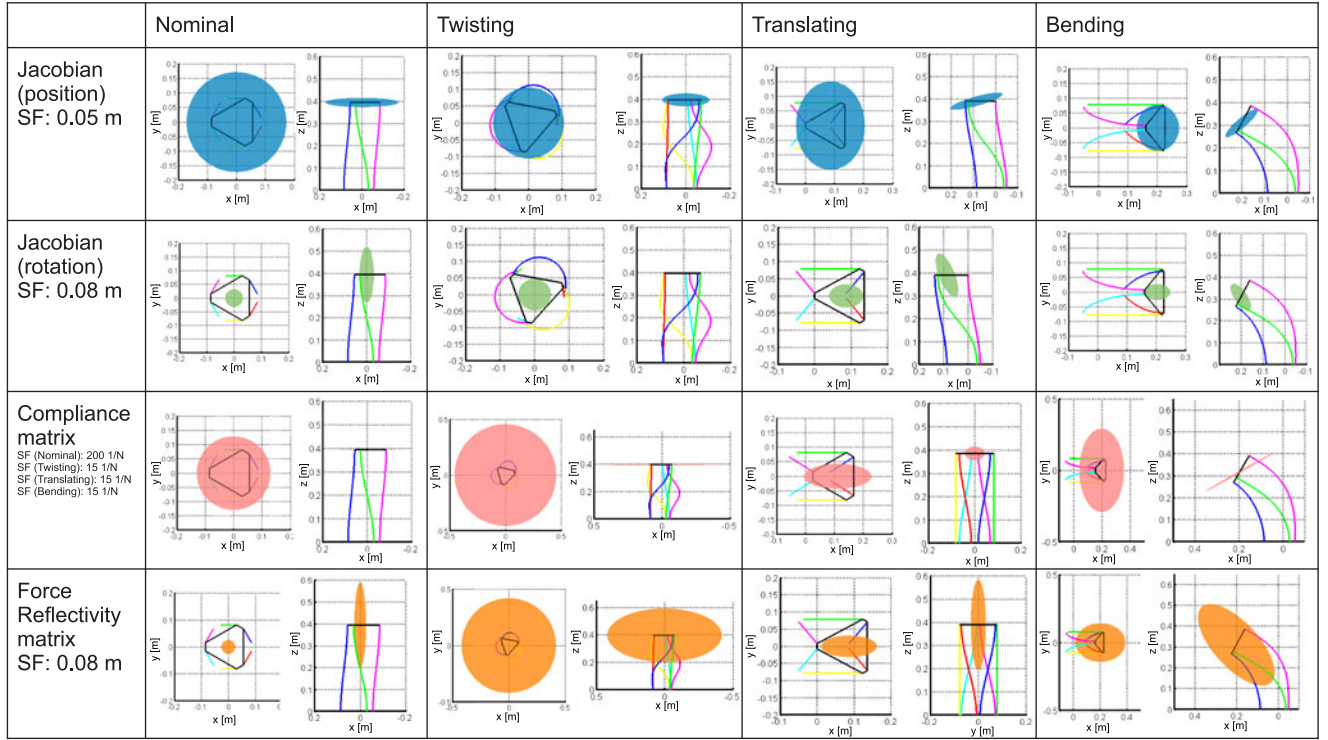


Fig. 6. Resulting ellipsoids when the manipulator is in three separate configurations, twisting about the z -axis, translating along the x -axis, and bending in the negative x -direction.

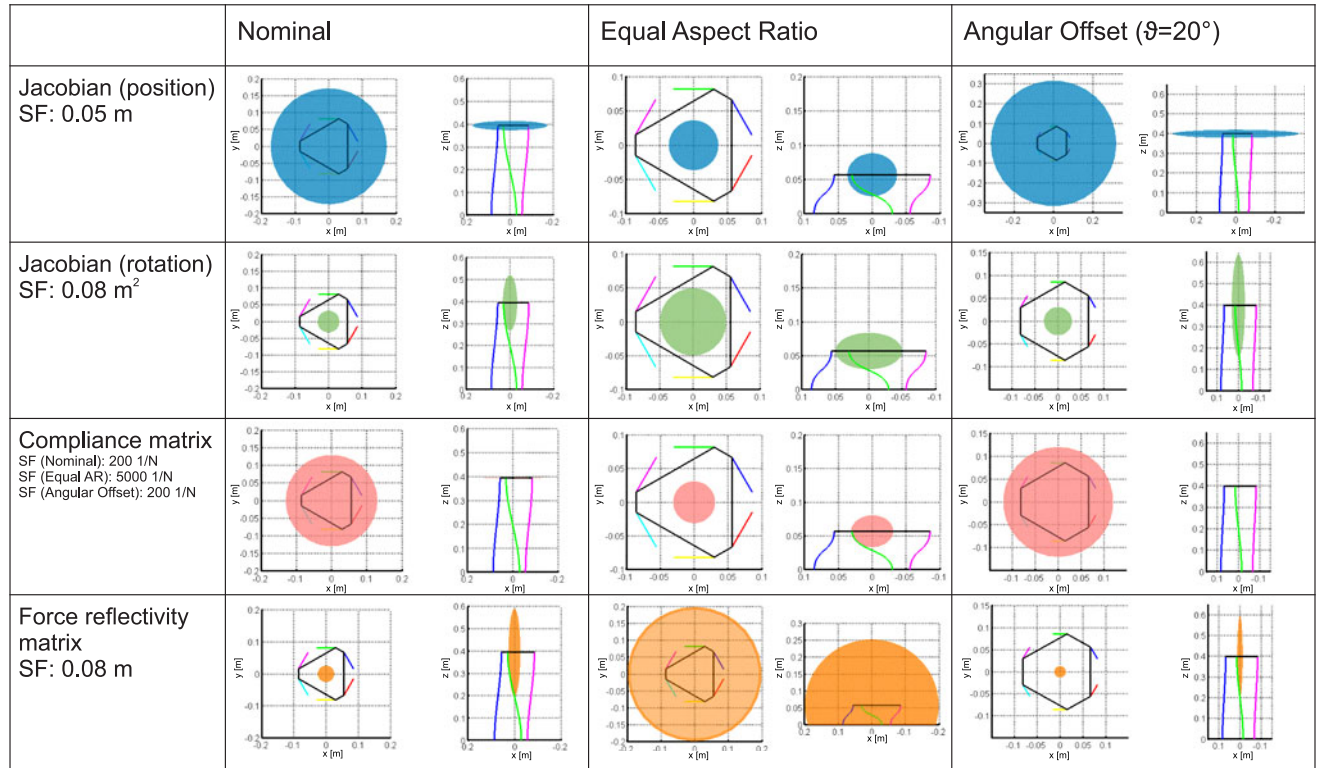


Fig. 7. Position (blue) and rotation (green) ellipsoids from the body Jacobian as well as the force displacement ellipsoid from the compliance matrix and the force reflectivity ellipsoid from the wrench reflectivity matrix.

position/rotation ellipsoid radius corresponds to the ability of the robot to move/rotate in the corresponding direction. A large radius in a particular direction means that a small amount of displacement in the actuator space is required for a relatively large amount of displacement in that direction in the Cartesian space.

This process can also be applied to the force/displacement portion of the compliance matrix and force portion of the wrench reflectivity matrix. Equation (25) contains the full compliance matrix related to linear and angular displacements and wrench. The displacement/force subblock (the upper 3×3 block, designated \mathbf{C}_f) of the compliance matrix is used to calculate the ellipsoid shown in Figs. 6 and 7. This reduction in dimension is again made for unit consistency and because a 6-D ellipsoid is difficult to visualize in 2-D projections.

Similarly, the force reflectivity ellipsoid is computed using the force/force subblock (the left $n \times 3$ block, designated \mathbf{W}_f) of the wrench reflectivity matrix in (25). This portion of the matrix involves only the tip forces and the actuation forces and ensures unit uniformity. These same matrices were used in the calculation of the indices reported in Table IV. The ellipsoid demonstrates the direction in which the forces are more or less “sensible” via transmission to the actuator loads. If the magnitude of the ellipsoid radius is large, a small change in the external force at the tip corresponds to a large change in the actuation forces that are sensed at the base of the link. If this is the case, the force would be more easily detected by the sensor.

D. Pose and Design Variations

In Fig. 6, the particular manipulator is represented in the nominal configuration (Column 1) along with three pose variations (Columns 2–4). The radii of each ellipsoid have units corresponding to the units of the respective matrices. In order to plot the ellipsoids in the Cartesian space, each ellipsoid has been scaled by a factor (SF) in order to convert the units to length and provide the best visualization for the plots. This scaling is arbitrary and has been applied to the ellipsoid uniformly over all three principle radii. The values and units for the scaling factors are shown in the figure.

1) *Nominal Configuration:* In the nominal configuration, the position manipulability ellipsoid shows that the manipulator is isotropic in the x - and y -directions. The z -axis radius is much smaller than the x and y indicating that the required actuator displacements are much higher to move in the z -direction. The rotational ellipsoid has a large radius in the z -direction compared to the x - and y -axes. This is consistent with the ease of twisting that is achieved in the axial direction versus the larger actuator displacement required to tilt to an equal angular displacement in the x - and y -directions. The scale factor of 200 1/N on the compliance matrix demonstrates that forces on the order of 1 N will displace the manipulator a distance on the order of 1 mm. The compliance ellipsoid also shows that the stiffness in the axial direction is much larger than in the x - and y -directions. The force reflectivity matrix shows that forces in the axial direction will be well reflected at the base, since the largest radius is in the axial direction.

2) *Twisting:* In Fig. 6, the second column shows the resulting kinetostatic ellipsoids when the manipulator is twisted about the z -axis. The position ellipsoid radius in the x - and y -directions is smaller. This would indicate that it is more difficult to move in the x - and y -directions when the manipulator is twisted. The rotation ellipsoid is flattened in the z -direction, which is expected, since the manipulator is already twisted in that direction. The length of the radius could potentially be used as an indicator of when the twisting limit is reached. The compliance ellipsoid radius in the x - and y -direction is significantly larger. This indicates that the robot is much less stiff in the x - and y -directions when it is twisted. The force reflectivity matrix is much larger and more isotropic, which means actuator forces are more sensitive to end-effector forces in this configuration.

3) *Translating:* The kinetostatic ellipsoids in the third column result from the manipulator being translated in the xy plane. All of the ellipsoids tilt. There are no significant changes in the size of the ellipsoids except for the compliance ellipsoid, which shrinks in the direction perpendicular to the plane of translation, indicating that the robot is stiffer in the direction perpendicular to its translation.

4) *Bending:* The fourth column of Fig. 6 shows the manipulator bent in the xz plane. Again, all the ellipsoids tilt. The position and compliance ellipsoids tilt in the opposite direction of the bending, while the rotation and force reflectivity tilt in the same direction. Both of the position and rotation ellipsoids shrink in response to the manipulator moving toward a singular configuration. The compliance matrix grows in the x - and y -directions, indicating that the manipulator is more flexible in the bent state in those directions. The force reflectivity ellipsoid also grows, which means that the forces at the tip are better transmitted to the actuators in this pose.

In Fig. 7, the manipulator is represented in the nominal configuration (Column 1) along with two design variations (Columns 2 and 3). The first column shows each ellipsoid while the manipulator is in the nominal configuration with all link lengths equal. The second column shows the same design but with an aspect ratio (relationship between the total length and the radius) of 1:1. The third column shows the same design with an increase in the angular displacement of the links both proximal and distal (from 10° to 20°).

5) *Equal Aspect Ratio:* The aspect ratio of the robot is the ratio of the radius r (distance from the center of the end effector to the link constraint holes) to the total length of the robot in the nominal straight configuration, L . In the nominal configuration, this ratio was 1:4.6. In Column 2 of Fig. 7, the ratio is 1:1. All of the ellipsoids are more isotropic than in the nominal configuration. However, the radius also decreased in all but the force reflectivity ellipsoid. The diameter of the compliance ellipsoid significantly decreased and required a much larger scaling factor in order to visualize the ellipsoid. From these results, it can be shown that a very short PCR is a very sensitive force sensor. However, the volume of the position and rotation ellipsoids are greatly decreased in the nominal configuration. This could indicate that the manipulator is more constrained in a shorter configuration. However, this was not the case for the force reflectivity ellipsoid. Instead of decreasing in size,

the ellipsoid increased in volume by 6000%, providing a larger range of sensible forces.

6) *Angular Offset*: The link angular offset is the angular displacement of the links from the equally spaced 120° lines dividing the circumference of the manipulator (see Fig. 5). In Column 1 of Fig. 7, $\vartheta = 10^\circ$, and in Column 3, $\vartheta = 20^\circ$ with a total angular offset of 40° between the flexible links. The positional ellipsoid shows a much larger diameter in the x - and y -directions. Since the scaling of the positional ellipsoid is constant, this translates to a larger Cartesian displacement for the same amount of actuator displacement. There is also a larger diameter in the z -direction for the rotational ellipsoid. This indicates that a greater degree of axial twisting is possible. There is no significant change in the compliance matrix in this simulation. There is a much smaller diameter in the x - and y -directions of the force reflectivity matrix, suggesting that this PCR design is a much less sensitive force sensor.

E. Matrix Metrics

The μ term in [19] and [32] of the form

$$\mu = \sqrt{\det(\mathbf{A}\mathbf{A}^T)} \quad (26)$$

is the most widely accepted measure for kinetostatic manipulability when applied to the Jacobian matrix. For the Jacobian matrix, μ measures the relative proximity of the current configuration to a singular configuration. If the matrix is square, it reduces to the absolute value of the determinant. For an arbitrary matrix, it generally corresponds to the notion of volume spanned by its columns. A value of 0 implies a configuration that is singular. This metric is also calculated for the compliance and force reflectivity matrices. The results are reported in Table IV for \mathbf{J}_p , \mathbf{J}_r , \mathbf{C}_f , and \mathbf{W}_f . The values for the force compliance matrix are close to zero. This is due to the high degree of axial stiffness (in the z -direction) when compared to the x - and y -directions from the inability to compress the links.

The second measure in the table, β , is the ratio of the largest and smallest singular values and measures the isotropy of the ellipsoid. It is an index of the directional uniformity of the ellipsoid that is independent of its size [32]. It can also be interpreted as the measure of accuracy with which the manipulator can generate output forces from actuator forces and workspace velocity from joint velocity [19]. The measure of isotropy has an upper bound of 1 and measures how close the ellipsoid is to a perfect sphere where all the eigenvalues would be equal.

When comparing the indices for the position and rotation ellipsoids in the nominal pose, β is not close to zero, which indicates that the robot is not singular in the configurations examined. This is consistent with previous findings of the nominal configuration in [39]. The compliance matrix is significantly skewed in the x - and y -directions, and this leads to a very low value for the isotropy. Examining β for the equal aspect ratio case in Table IV, it is evident that all the matrices are extremely well conditioned in this configuration. The μ value for the angular displacement case shows that the volume of the force reflectivity matrix decreased significantly.

F. Nondimensional Analysis

We would like to obtain a generally applicable function that relates how the link lengths, hole-pattern radius, link bending stiffness, and hole-pattern angular offset affect the end-effector output compliance matrix (specifically the transverse compliance, $C_{xx} = \frac{\partial p_x}{\partial f_x}$, which is the first diagonal element in the compliance matrix) for any Stewart–Gough PCR in the nominal configuration. Knowing how to select physical parameters that correspond to a specific stiffness can aid in designing robots to interact with specific stiffness requirements, such as probing soft tissue or working close to a human collaborator. To obtain such a generalized relationship, we used the Buckingham Pi method [49] to find three dimensionless groups. For our analysis, there are five problem parameters (L , r , ϑ , EI , and C_{xx}) and two physical dimensions in the problem (length and force). According to the Buckingham Pi theory, there are then three dimensionless groups.

The first two groups are the aspect ratio (radius of the robot divided by the length) and the angular offset of the flexible links in degrees

$$\Pi_1 = \vartheta$$

$$\Pi_2 = \frac{r}{L}.$$

A third dimensionless group can be written in terms of the compliance, stiffness, and length

$$\Pi_3 = \frac{C_{xx}EI}{L^3}.$$

Therefore, some function exists that relates the dimensionless groups as

$$\frac{C_{xx}EI}{L^3} = f\left(\vartheta, \frac{r}{L}\right). \quad (27)$$

If the design required increased or decreased compliance, these nondimensional groups provide insight to how to scale the physical parameters of the manipulator. This formulation reveals that if all the length dimensions of the manipulator (r , L , and link diameter through I) are scaled by a factor κ , the compliance C_{xx} will be scaled by $\frac{1}{\kappa}$. Also, if the length and radius of the manipulator are both scaled by a factor κ , then the compliance will increase by a factor of κ^3 . These general rules equally apply to any other element of the compliance matrix, and also to the inverse of the input stiffness matrix \mathbf{K} , since we could have chosen any scalar compliance for the formation of Π_3 .

To determine a functional approximation for (27) above, we used the mechanics model to simulate a range of aspect ratios and angular offsets and calculated the resulting C_{xx} . The angular offset ranged from 0° to 30° (i.e., from designs with leg pairs coincident to designs with equally spaced, straight legs) and the aspect ratio ranged from 0.0625 to 0.4. The values were plotted against Π_3 and fitted to a function using the Eureka Pro tool from Nutonian Inc., which uses a genetic algorithm to find an appropriate functional form that fits a set of data. We converged

Non-dimensional Analysis in the Nominal Configuration

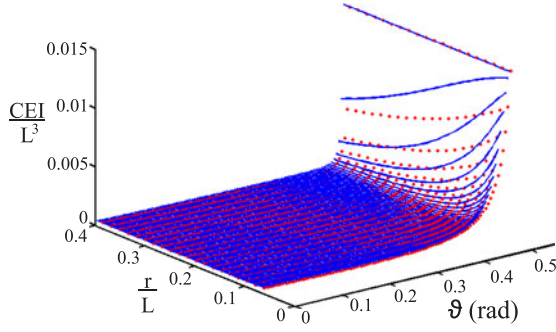


Fig. 8. Results of the fitted data [see (28)] are shown here as red diamonds and the simulation data are shown in the blue line. The sudden change in compliance near $\vartheta = 30^\circ$ is an interesting result of this analysis.

on an equation with the form

$$\frac{CEI}{L^3} = c_1 + c_2\vartheta + c_3\vartheta^2 + \frac{c_4\vartheta^4}{c_5\vartheta \frac{r}{L} + c_6 + c_7 \frac{r}{L}} + c_8\vartheta^7 \quad (28)$$

where

$$\begin{aligned} c_1 &= 0.000489911011960653 \\ c_2 &= -7.708585607305636e \times 10^{-4} \\ c_3 &= 0.001122924359743 \\ c_4 &= -0.019046236046962 \\ c_5 &= 57.295779513082323 \\ c_6 &= -0.0923645619398372 \\ c_7 &= -30.0023461726314 \\ c_8 &= -0.175434258024175. \end{aligned}$$

The genetic algorithm provides the user options to balance complexity of the resulting equation and a better fit of the data. This equation best fits the experimental data. While some of the coefficients are small in magnitude, they are multiplied by exponential terms, which increases their contribution to the overall equation. This polynomial produced an R-squared value of 0.966 for the data collected and reflected the expected compliance of the manipulator when given an aspect ratio and an angular displacement of the flexible links from the midline (see Fig. 5). We measured the percent error between the dataset and the fitted equation and found a maximum percent error of 25.4%. The results of the dimensional analysis simulation are shown in Fig. 8. It is important to note that this function is valid only for the limits of the simulation data and will decrease in accuracy if used outside these limits.

There is a hyperbolic relationship between the angular offset of the flexible links and the compliance term. This curve is sharpened when the aspect ratio of the robot is increased. Due to the nondimensional nature of the analysis, these findings and this equation apply to all Stewart–Gough PCR robots, regardless of size or materials. The findings will facilitate robot design without requiring the full kinetostatic model.

TABLE V
FORCE APPLICATION [N] PER CONFIGURATION

Pose/Variation	$x = 1 \text{ mm}$	$y = 1 \text{ mm}$	$z = 1 \text{ mm}$
Nominal	[1.54 0 0.01]	[0 1.54 0]	[0.01 0 109.5]
Aspect Ratio	[160.5 0 1.5]	[0 160.4 -0.4]	[0.8 -0.02 210.4]
Angular Offset	[1.65 0 0.05]	[0 1.65 -0.01]	[0.04 0.01 407.0]
Twisting	[0.03 0 0]	[0 0.03 0]	[0 0 3.82]
Translating	[2.36 0 9.37]	[0 0.1 0]	[9.35 0 37.7]
Bending	[0.81 0 1.28]	[0 0.05 0]	[1.29 0 2.36]

G. Force Application

It is important to know the end-effector's force application capacity in different directions and for different configurations in order to assess the manipulator's ability to perform certain tasks. In order to assess the force application capacity, the displacement/force (upper 3×3) subblock of the compliance matrix can be used to solve for the force required to produce any small linear displacement. Using this approach, we analyzed the 3-D forces required to produce a displacement of 1 mm in the x -, y -, and z -directions (in the local end-effector frame) for a manipulator in the six pose and geometry variations examined in this section. The results are presented in Table V. In the nominal configuration, the x and y displacement forces are symmetrical, while the z force is quite large in comparison. This agrees with the representation of the compliance matrix in Figs. 6 and 7. The equal aspect ratio values demonstrate the scaling of the force application capacity when the manipulator is shortened. If the manipulator is shortened 87%, then the force it can apply before displacement of 1 mm increases by a factor of 2 in the z -direction and by a factor of 100 in the x - and y -directions. The angular offset increase results in only marginal increases in force application capacity in the x - and y -directions but increases the capacity in the z -direction by a factor of 4. Twisting is shown to greatly decrease the stiffness in the x - and y -directions and increase it slightly in the z -direction. Translating in the xz plane greatly reduces the stiffness in the y -direction. Bending in the xz plane also decreases the stiffness in the y -direction.

IV. FORCE-SENSING EXPERIMENTS

In Section II-E, we presented three different model formulations for force sensing with parallel continuum manipulators. In choosing a force-sensing approach, it is important to understand how the errors in the input values will affect the accuracy of the sensed wrench. In order to compare the available options for force-sensing methods, the three sensing formulations were evaluated to investigate error propagation from the actuator positions, actuator forces, and pose.

In $F_{q,\tau}$, error could arise from the actuator force measurement or the commanded actuator variables. Solving the second equation in (20) for the wrench gives

$$\delta \mathbf{w} = \mathbf{W}^{-1} \delta \boldsymbol{\tau} - \mathbf{W}^{-1} \mathbf{K} \delta \mathbf{q}. \quad (29)$$

In order to analyze the effect of errors in actuator displacement and force measurement, we assume Gaussian distributions in the input and output variables and define the input covariance matrix, which is then transformed through the above equation

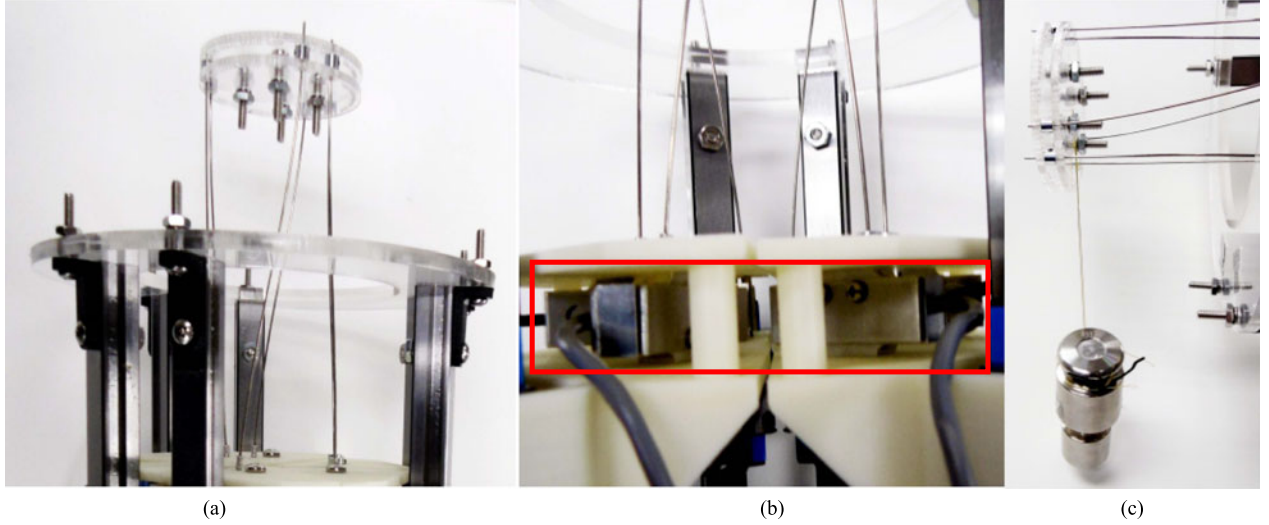


Fig. 9. (a) Manipulator consisting of six flexible spring tempered carbon steel wire rods (AISI 302/304 stainless steel) connected in a conventional Stewart–Gough configuration. (b) Omega load cells are connected directly to the flexible rods to measure the actuation forces and translated by linear rails and carriages. (c) 300-g weight was hung from the centroid of the end effector for each of the force application experiments.

to provide an output covariance [50]. This has the form

$$\Sigma_w = [\mathbf{W}^{-1} \quad -\mathbf{W}^{-1}\mathbf{K}] \begin{bmatrix} \Sigma_\tau & \mathbf{0} \\ \mathbf{0} & \Sigma_q \end{bmatrix} [\mathbf{W}^{-1} \quad -\mathbf{W}^{-1}\mathbf{K}]^T \quad (30)$$

where the Σ_τ and Σ_q terms are the input covariances of the actuation forces and actuation variables, respectively. We assume that the error of each input is independent and uncorrelated so that these are both diagonal matrices.

The covariance is based on the range of accuracy that is estimated for each input. The square root of the variance of the error can be tripled to provide a range of error that contains the 95th percentile for the Gaussian distribution. Therefore, the estimated maximum error range can be divided by 3 and squared to arrive at the covariance value. The diagonal elements of the output covariance matrix, Σ_w , can be rooted and multiplied by 3 to find the 95th percentile range of error for tip wrench. For an input range of 0.1 N for τ (estimated from our force sensor data in Section IV-C) and 0.5 mm for q (estimated from linear actuator repeatability), the maximum range for force errors using the actuation based force-sensing method, $F_{q,\tau}$, is 0.0136 N in the nominal configuration with a moment error range of less than $1e^{-4}$ N·m. We note that this error estimate is pose dependent, since it uses the linearized matrices about the current pose.

The generalized deflection-based force-sensing method, $F_{g,q}$, for a PCR would use

$$\delta \mathbf{w} = \mathbf{C}^{-1}(\mathbf{g}_e^{-1} \delta \mathbf{g}_e)^\vee - \mathbf{C}^{-1} \mathbf{J} \delta \mathbf{q}. \quad (31)$$

Here, the covariance matrix contains ranges for pose accuracy and link length accuracy. For values of 0.2 mm (estimated from accuracy of commercially available 3-D image tracking systems) and 1 mm for the pose and link lengths error ranges, the resulting force error range is 1.4×10^{15} N. This large error range is due to \mathbf{C} being close to singular in this particular configuration. The intuition behind this result is that deflection-based wrench sensing is only effective for sufficiently compliant objects, and there is very little deflection when the robot is in

the straight nominal configuration and a vertical force is applied. This will mean that the $F_{g,q}$ problem is ill-posed enough to make numerical convergence difficult in this case. The third method of force sensing, $F_{g,\tau}$, estimates an even larger error range for tip wrench with the same values for error range used previously. These results indicate that the $F_{q,\tau}$ formulation (actuation based) is the best conditioned force-sensing approach for our parallel continuum manipulator prototype. Note that this is not a general result, as one could envision a robot design, which is significantly compliant in all directions, but has poorly conditioned reflection of forces to the actuators. In this case, deflection-based force sensing would be a better choice than actuation-based.

A. Manipulator Construction

The manipulator consists of six flexible spring tempered carbon steel wires (AISI 302/304 stainless steel) with a stated diameter of 1.04 mm. The overall length is 145 mm with a radius of 32.9 mm and an angular offset of 8° . The distal connections are torsionless with a set screw mounting. The force sensors are connected to the wires via 3-D printed interface parts that transfer the axial force directly to the sensor. The sensors are mounted to a steel slide carriage driven by a Firgelli L16 linear actuator. The linear actuators change the position of each wire base to create six-DOF motion of the end effector. No base plate is used and the proximal connection points are torsionless set screw connections. The design and construction are similar to previous systems [7], [39], [40], but this configuration removes the base platform in order to eliminate friction between the flexible links and the through holes, which can increase error in force estimation. The physical system used in the experiments is shown in Fig. 9.

B. Repeatability

The repeatability of the force sensor measurements within the open-loop robot system was evaluated by placing the manipula-

tor in the nominal configuration and actuating to eight different positions and then back to the nominal pose while measuring data from the force sensors. This resulted in nine instances of nominal configuration measurements with six load cells each. The average distance from the mean sensor reading in the nominal configuration was 0.15 N for all six sensors. The specified repeatability of the sensors is $\pm 0.05\%$ of the load, and there is no specified repeatability for the data acquisition. The load on each sensor in these configurations is due to the manipulation of the robot and, therefore, can only be estimated by the sensing method. This provides an estimation of the repeatability of the force sensors. Note that this measurement does not contain any friction terms due to the lack of a base plate and no sliding contact of the flexible links.

C. Data Collection

In order to validate the force-sensing capabilities of the manipulator, the actuation force applied to each link was recorded with Omega-LC703 load cells. These load cells were rigidly attached to the flexible links and reflect the internal axial force of the link at the proximal end. These measurements are then used as input, along with the commanded link positions, to the force-sensing model ($F_{q,\tau}$) to calculate an estimate of the external forces applied at the tip of the manipulator. The measurements were taken while the robot was in nine different positions [nominal, tilted (clockwise and counterclockwise about the y -axis), twisted ($+z$ and $-z$), translated in the xy plane ($+x$ and $-x$), and bent (clockwise and counterclockwise about the y -axis)) with a 300-g calibration weight hanging from the center of the end effector via Kevlar thread. This measurement was taken with the forces applied in the positive x , then the negative y , and, finally, the negative z -directions. This resulted in 27 cases of three-DOF force application symmetric to the global frame (twisting in the positive z and negative z -directions, etc.). In the nominal configuration, the readings from the load cells are assumed to be zero in order to calibrate the sensor readings. The manipulator was actuated to the previously described configurations with the weight hanging freely from the centroid, and measurements from all six load cells were taken. Then, the manipulator was returned to the nominal configuration with the weight removed, and measurements were taken again to ensure proper zeroing of the load cells.

D. Data Analysis

The load cell measurements were collected with an Omega DAQ-USB-2401 system [51]. Each measurement was taken for a minimum of 1 min at each position to ensure a steady-state reading. The force data signal was filtered with a built-in Butterworth filter in MATLAB using the `butter()` command to remove the high-frequency noise of the sensor. Once the data were filtered, the zero values were subtracted from the weighted values to find the actuator loads. To analyze the data, the known load was compared to the estimated load calculated using the force-sensing algorithm ($F_{q,\tau}$). The absolute value of the difference between the magnitudes of the known load and the estimated load M_e and the angular distance between the two

vectors, Θ_e , were calculated with

$$\begin{aligned} M_e &= ||\mathbf{F}_t|| - ||\mathbf{F}_{\text{est}}|| \\ \Theta_e &= \cos^{-1} \left(\frac{\mathbf{F}_t \cdot \mathbf{F}_{\text{est}}}{||\mathbf{F}_t|| ||\mathbf{F}_{\text{est}}||} \right) \end{aligned} \quad (32)$$

where \mathbf{F}_t is the known force of the hanging weight and \mathbf{F}_{est} is the estimated force from the sensing algorithm. The percent error, shown as %, was calculated by dividing the magnitude of the error vector by the magnitude of the known load vector. The results of the force-sensing experiments with no calibration are shown in Table VI.

E. Stiffness Calibration

The nominal Young's Modulus for AISI 302/304 is 193 GPa. We measured the diameter of the rods and found agreement with their nominal diameter of 1.04 mm. Thus, the nominal bending stiffness (flexural rigidity) for the links used in this manipulator is $0.0110 \text{ N}\cdot\text{m}^2$. To more accurately determine the flexural rigidity, we performed an experimental calibration of the Young's Modulus using a simple cantilevered bending test with a rod of the same diameter and material as the links in the PCR. The rod was clamped at one end with a 16-cm cantilevered length extending horizontally, and weights of 10, 20, 50, and 100 g were hung from its tip. For each case, we manually measured the tip deflection in the direction of the load. We chose a calibrated E value by minimizing the least-squares error between the measured tip deflection and the predicted deflection of the Cosserat rod model. Our calibrated value for E is 161 GPa, which results in a bending stiffness of $0.0092 \text{ N}\cdot\text{m}^2$. This value was used to re-evaluate all experimental wrench sensing data the wrench estimate, and the results are presented in Table VI. While the mean magnitude error of 0.35 N was not improved by the calibration, the mean directional error was improved by 1.5° . The relatively low change in the error statistics in response to a 17% change in E suggests that actuation-based wrench estimates are actually not very sensitive to the value of E . In contrast, deflection-based wrench estimates would vary linearly with E .

F. Results

The median difference in the magnitudes between the estimated force and the known force was 0.26 N in the uncalibrated dataset and 0.23 N in the calibrated dataset. Since this is higher than our estimated error of 0.0136 N based on sensor resolution, other errors in construction and load application likely affected the measurement of the actuation loads and the force estimation. The median directional error in the uncalibrated dataset was 12.47° and 12.13° in the calibrated dataset. The highest errors occurred in the case of pure translation. Possible sources of error in force estimation include inaccuracies in the specification of the nominal link lengths and/or positional inaccuracies of the linear motion system, and mechanical tolerances in the construction of the manipulator and linear motion system. The linear actuators have a backlash of 0.5 mm, and the linearity of the potentiometer is less than 2%. Other sources include elastic

TABLE VI
FORCE ESTIMATION EXPERIMENTS

\mathbf{F}_t	Configuration	Nominal EI (EI = 0.0110 N·m ²)				Bending Test Calibrated EI (EI = 0.0092 N·m ²)			
		\mathbf{F}_{est} [N]	M_e [N]	%	Θ_e [°]	\mathbf{F}_{est} [N]	M_e [N]	%	Θ_e [°]
[2.94 0 0]	Nominal	[2.97 0.20 0.22]	0.04	1.31	5.69	[2.97 0.20 0.22]	0.04	1.33	5.64
	Twisting	[2.57 -0.21 -0.19]	0.35	12.00	6.19	[2.59 -0.20 -0.19]	0.34	11.63	6.05
		[2.89 0.02 -0.94]	0.10	3.2	18.0	[2.25 0.30 0.22]	0.67	22.65	9.43
		[2.39 0.56 0.22]	0.48	16.30	14.05	[2.64 -0.25 -1.74]	0.23	7.95	33.66
	Tilting	[2.84 0.03 -0.63]	0.04	1.27	12.47	[3.06 0.21 -0.62]	0.19	6.43	12.13
		[3.04 -0.25 -1.74]	0.57	19.47	30.07	[0.14 -2.72 -0.44]	0.18	6.28	9.73
	Translating	[2.26 0.24 1.24]	0.35	11.92	29.20	[0.57 -2.67 0.06]	0.22	7.34	12.14
		[3.09 0.22 -0.62]	0.21	7.30	12.04	[-0.14 -2.63 -0.22]	0.30	10.12	5.61
		[2.70 0.30 -0.39]	0.19	6.61	10.29	[0.57 -3.13 -0.60]	0.30	10.11	14.84
	Bending	[0.14 -2.72 -0.44]	0.19	6.31	9.73	[0.10 -2.34 -0.63]	0.52	17.65	15.31
		[0.57 -2.68 0.06]	0.20	6.85	12.10	[-0.03 0 -2.82]	0.12	4.11	0.56
		[-0.15 -2.57 -1.39]	0.02	0.60	28.54	[-0.01 0.10 -2.45]	0.49	16.77	2.33
[0 -2.94 0]	Nominal	[0.14 -2.72 -0.44]	0.19	6.31	9.73	[0.10 -2.34 -0.63]	0.52	17.65	15.31
	Twisting	[0.57 -2.68 0.06]	0.20	6.85	12.10	[-0.03 0 -2.82]	0.12	4.11	0.56
		[-0.15 -2.57 -1.39]	0.02	0.60	28.54	[-0.01 0.10 -2.45]	0.49	16.77	2.33
		[-0.35 -2.65 -0.22]	0.26	8.99	8.87	[-0.25 0.47 -2.95]	0.06	1.91	10.25
	Tilting	[0.47 -2.51 -1.37]	0.04	1.43	29.97	[0.81 -0.35 -3.56]	0.73	24.80	13.94
		[0.99 -3.17 -0.60]	0.43	14.67	20.08	[-0.32 0.04 -3.42]	0.49	16.57	5.41
		[-0.77 -2.18 0.84]	0.49	16.56	27.60	[2.89 0.04 -0.94]	0.10	3.37	17.97
	Translating	[0.12 -2.33 -0.63]	0.52	17.79	15.42	[2.63 0.02 -0.63]	0.24	8.03	13.40
		[0.23 -1.95 -0.43]	0.93	31.61	14.07	[2.67 0.23 1.24]	0.01	0.44	25.32
		[-0.03 0.00 -2.82]	0.12	4.11	0.56	[2.71 0.28 -0.39]	0.19	6.43	10.12
	Bending	[-0.02 0.12 -2.45]	0.49	16.74	2.76	[-0.15 -2.59 -1.39]	0	0.13	28.33
		[0.33 -0.04 -2.78]	0.14	4.81	6.72	[0.26 -2.50 -1.37]	0.08	2.68	29.15
		[-0.44 0.51 -2.95]	0.08	2.89	12.91	[-0.36 -2.18 0.84]	0.58	19.59	22.73
[0 0 -2.94]	Nominal	[0.57 -0.01 -2.88]	0.01	0.38	11.17	[0.24 -1.93 -0.43]	0.95	32.27	14.25
	Twisting	[1.20 -0.37 -3.56]	0.84	28.45	19.44	[0.32 -0.03 -2.78]	0.14	4.83	6.63
		[-1.06 0.23 -1.33]	1.22	41.62	39.13	[0.37 0.01 -2.88]	0.04	1.46	7.31
		[-0.31 0.04 -3.42]	0.49	16.55	5.28	[-0.66 0.23 -1.33]	1.44	48.89	27.62
	Tilting	[0.28 0.29 -3.60]	0.68	23.00	6.51	[0.29 0.28 -3.60]	0.68	22.97	6.40
		Max	1.22	41.62	39.13	Max	1.44	48.89	33.66
		Mean	0.35	11.96	15.14	Mean	0.35	11.73	13.56
		Median	0.26	8.99	12.47	Median	0.23	7.95	12.13
	Bending								

deformation of the end-effector plate, which is assumed to be a rigid body in the model and potential small plastic deformation of the links.

V. CONCLUSION

This paper provided a general kinetostatics modeling framework for parallel continuum manipulators, including general proximal and distal boundary conditions and six different model formulations useful for various types of control and sensing. We provided the linearization of this framework, identified kinetostatic matrices, and quantified performance expectations related to the capabilities of PCRs in different designs and configurations. We provided an investigation of the effects of design and configuration on the manipulability and force-sensing potential of the parallel continuum manipulator. We found that a decrease in the overall length-to-width ratio of the manipulator decreases the anisotropy of the ellipsoids. We also formulated a nondimensional relationship for manipulator compliance. These analyses can be expanded to other continuum robots to provide similar information.

We also investigated the force-sensing accuracy of our prototype manipulator with a model-based approach that uses actuator variables and actuator forces. The low force-sensing error demonstrated that accurate actuation-based force sensing is feasible for parallel continuum manipulators of the Stewart–Gough type. These results are encouraging for future systems with higher accuracy in linear motion and force measurement.

However, one limitation of our experiments is that we did not investigate the effect of frictional interference with a base plate. Future work should quantify the level to which transmission friction reduces force-sensing accuracy.

The modeling, analysis, and force-sensing results in this paper will be instrumental to fully realize the benefits of PCRs for applications in safe human–robot interaction and robotic surgery. Future topics building on this investigation will include stiffness control, haptic feedback, and further miniaturized prototypes that can apply all these results to surgical applications.

APPENDIX A

NOMENCLATURE

- * in reference state.
- ' Derivative with respect to s .
- \wedge Converts \mathbb{R}^3 to $\mathfrak{so}(3)$ and \mathbb{R}^6 to $\mathfrak{se}(6)$:

$$\hat{\mathbf{u}} = \begin{bmatrix} 0 & -u_3 & u_2 \\ u_3 & 0 & -u_1 \\ -u_2 & u_1 & 0 \end{bmatrix}$$

$$\begin{bmatrix} \hat{\mathbf{v}} \\ \hat{\mathbf{u}} \end{bmatrix} = \begin{bmatrix} 0 & -u_3 & u_2 & v_1 \\ u_3 & 0 & -u_1 & v_2 \\ -u_2 & u_1 & 0 & v_3 \\ 0 & 0 & 0 & 0 \end{bmatrix}.$$

\vee

Inverse of the \wedge operation. $(\hat{\mathbf{u}})^\vee = \mathbf{u}$.

$s \in \mathbb{R}$	Reference length parameter.	\mathbf{C}	Body-frame compliance matrix.
$\mathbf{p}_i(s) \in \mathbb{R}^3$	Position of the i th link as a function of length.	\mathbf{K}	Input stiffness matrix mapping changes in joint position to changes in actuator forces.
$\mathbf{R}_i(s) \in \text{SO}(3)$	Orientation of the i th link as a function of length.	\mathbf{W}	Wrench reflectivity matrix mapping changes in applied wrench to changes in actuation forces.
$\mathbf{g}_i(s) \in \text{SE}(3)$	Homogeneous transformation containing $\mathbf{R}_i(s)$ and $\mathbf{p}_i(s)$ (the “body frame”).	\mathbf{B}_τ	Matrix mapping changes in boundary condition vector and actuation forces.
$\mathbf{v}_i(s) \in \mathbb{R}^3$	Linear rate of change of $\mathbf{g}_i(s)$ with respect to s in the body-frame coordinates ($\mathbf{v}_i(s) = \mathbf{R}_i^T(s)\mathbf{p}'_i(s)$).	\mathbf{B}_q	Matrix mapping changes in boundary condition vector and actuation variables.
$\mathbf{u}_i(s) \in \mathbb{R}^3$	Angular rate of change of $\mathbf{g}_i(s)$ with respect to s in body-frame coordinates.	\mathbf{B}_w	Matrix mapping changes in boundary condition vector and external wrench.
$\mathbf{n}_i(s)$	Internal force in the link expressed in global coordinates.	\mathbf{B}_{gc}	Matrix mapping changes in boundary condition vector and end-effector pose.
$\mathbf{m}_i(s)$	Internal moment in the link expressed in global coordinates.	\mathbf{B}_γ	Matrix mapping changes in boundary condition vector and unknown proximal variables.
\mathbf{f}_i	External distributed force.	$\mathbf{\Gamma}$	Linear mapping between unknown proximal variables and the vector containing actuation variables and wrench.
\mathbf{l}_i	External distributed moment.	μ	Matrix measurement of proximity to a singularity.
$\mathbf{K}_{se,i}$	Shear and extension stiffness matrix.	β	Ellipsoid measurement of isotropy.
$\mathbf{K}_{bt,i}$	Bending and torsion stiffness matrix.	r	Radius of manipulator end-effector platform.
A_i	Area of the link cross section.	L	Total length of the manipulator.
G_i	Shear modulus of link material.	ϑ	Angular displacement of link ends from dividing lines at 0° , 120° , and 240° .
E_i	Young’s modulus of link material.	\mathbf{K}_o	Output stiffness matrix, $\mathbf{K}_o = \mathbf{C}(1 : 3, 1 : 3)$.
I_i	Second moment of area of link cross section about the local x - and y -axis.	\mathbf{F}_t	Known force applied to the end-effector centroid.
J_i	Polar moment of area about the local z -axis.	\mathbf{F}_{est}	Sensed force at the end-effector centroid based on actuator force measurements.
l_i	Length of individual links.	M_e	Magnitude of the difference between the known load and the estimated load in Newtons.
\mathbf{F}	External force vector applied at the end-effector centroid expressed in global coordinates.	Θ_e	Angular distance between the two vectors in degrees.
\mathbf{M}	External moment vector applied at the end-effector centroid expressed in global coordinates.		
\mathbf{w}	External wrench vector ($\mathbf{w} = [\mathbf{F}^T \mathbf{M}^T]$).		
\mathbf{p}_e	End-effector position in global coordinates.		
\mathbf{R}_e	End-effector orientation in global coordinates.		
\mathbf{g}_e	End-effector pose in global coordinates.		
$\mathbf{R}_{\alpha,i}$	User-defined offset orientation at the distal end of each link.		
$\boldsymbol{\alpha}_i \in \mathbb{R}^3$	Angular displacement vector defining $\mathbf{R}_{\alpha,i}$		
$\boldsymbol{\rho}_i$	Position vector relating end-effector centroid and individual links in local coordinates.		
\mathbf{q}_i	Actuation variable vector defined as the z -axis position of the base of the link in the global frame.		
l_i	Length of link above the base plate.		
L_i	Total length of the link.		
$\boldsymbol{\theta}_i$	Angular displacement vector defining $\mathbf{R}_i(0) = \mathbf{R}(\boldsymbol{\theta}_i)$.		
ϕ_i	User-defined initial axial rotation of the link at the point of attachment to the actuator.		
\mathbf{y}_i	Vector of all link variables ($\mathbf{y}_i = \mathbf{g}_i, \mathbf{n}_i, \mathbf{m}_i$).		
\mathbf{y}'_i	Vector containing all differential equations for n links.		
\mathbf{b}	Vector containing distal boundary conditions and static equilibrium equations.		
$\boldsymbol{\mu}$	Vector containing unknown proximal variables.		
$\boldsymbol{\tau}$	Vector of actuation forces for each link.		
\mathbf{J}	Body-frame Jacobian.		

REFERENCES

- [1] R. J. Webster and B. A. Jones, “Design and kinematic modeling of constant curvature continuum robots: A review,” *Int. J. Robot. Res.*, vol. 29, pp. 1661–1683, 2010.
- [2] J.-P. Merlet, *Parallel Robots*, vol. 74. New York, NY, USA: Springer, 2012.
- [3] J. Ding, R. E. Goldman, K. Xu, P. K. Allen, D. L. Fowler, and N. Simaan, “Design and coordination kinematics of an insertable robotic effectors platform for single-port access surgery,” *IEEE/ASME Trans. Mechatronics*, vol. 18, no. 5, pp. 1612–1624, Oct. 2013.
- [4] N. Simaan, “Snake-like units using flexible backbones and actuation redundancy for enhanced miniaturization,” in *Proc. IEEE Int. Conf. Robot. Autom.*, 2005, pp. 3012–3017.
- [5] N. Simaan, R. Taylor, and P. Flint, “A dexterous system for laryngeal surgery,” in *Proc. IEEE Int. Conf. Robot. Autom.*, 2004, vol. 1, pp. 351–357.
- [6] J. Burgner-Kahrs, D. C. Rucker, and H. Choset, “Continuum robots for medical applications: A survey,” *IEEE Trans. Robot.*, vol. 31, no. 6, pp. 1261–1280, Dec. 2015.
- [7] A. L. Orekhov, C. B. Black, J. Till, S. Chung, and D. C. Rucker, “Analysis and validation of a teleoperated surgical parallel continuum manipulator,” *IEEE Robot. Autom. Lett.*, vol. 1, no. 2, pp. 828–835, Jul. 2016.
- [8] A. L. Orekhov, C. E. Bryson, J. Till, S. Chung, and D. C. Rucker, “A surgical parallel continuum manipulator with a cable-driven grasper,” in *Proc. 37th Annu. Int. Conf. IEEE Eng. Med. Biol. Soc.*, 2015, pp. 5264–5267.

- [9] M. Veloso *et al.*, "Cobots: Collaborative robots servicing multi-floor buildings," in *Proc. IEEE/RSJ Int. Conf. Intell. Robots Syst.*, Oct. 2012, pp. 5446–5447.
- [10] R. E. Goldman, A. Bajo, and N. Simaan, "Compliant motion control for multisegment continuum robots with actuation force sensing," *IEEE Trans. Robot.*, vol. 30, no. 4, pp. 890–902, Aug. 2014.
- [11] 2011. [Online]. Available: <http://www.festo.com/net/SupportPortal/Files/46268>
- [12] N. Simaan, R. Taylor, and P. Flint, "High dexterity snake-like robotic slaves for minimally invasive telesurgery of the upper airway," in *Proc. Int. Conf. Med. Image Comput. Comput.-Assisted Intervention*, 2004, pp. 17–24.
- [13] N. Simaan, R. Taylor, A. Hillel, and P. Flint, "Minimally invasive surgery of the upper airways: Addressing the challenges of dexterity enhancement in confined spaces," in *Surgical Robotics—History, Present and Future Applications*, Russell A. Faust, Ed. New York, NY, USA: Nova Science, 2007, pp. 261–280.
- [14] D. B. Camarillo, C. F. Milne, C. R. Carlson, M. R. Zinn, and J. K. Salisbury, "Mechanics modeling of tendon-driven continuum manipulators," *IEEE Trans. Robot.*, vol. 24, no. 6, pp. 1262–1273, Dec. 2008.
- [15] W. McMahan *et al.*, "Field trials and testing of the OctArm continuum manipulator," in *Proc. IEEE Int. Conf. Robot. Autom.*, 2006, pp. 2336–2341.
- [16] D. Trivedi, A. Lotfi, and C. Rahn, "Geometrically exact models for soft robotic manipulators," *IEEE Trans. Robot.*, vol. 24, no. 4, pp. 773–780, Aug. 2008.
- [17] P. E. Dupont, J. Lock, B. Itkowitz, and E. Butler, "Design and control of concentric-tube robots," *IEEE Trans. Robot.*, vol. 26, no. 2, pp. 209–225, Apr. 2010.
- [18] D. C. Rucker, B. A. Jones, and R. J. Webster, "A geometrically exact model for externally loaded concentric-tube continuum robots," *IEEE Trans. Robot.*, vol. 26, no. 5, pp. 769–780, Oct. 2010.
- [19] S. Patel and T. Sobh, "Manipulator performance measures—A comprehensive literature survey," *J. Intell. Robot. Syst.*, vol. 77, nos. 3/4, pp. 547–570, 2015. [Online]. Available: <http://dx.doi.org/10.1007/s10846-014-0024-y>
- [20] J.-P. Merlet, "Jacobian, manipulability, condition number, and accuracy of parallel robots," *J. Mech. Des.*, vol. 128, no. 1, pp. 199–206, 2006.
- [21] G. Gogu, *Structural Synthesis of Parallel Robots*. New York, NY, USA: Springer, 2008.
- [22] X.-J. Liu, C. Wu, and J. Wang, "A new index for the performance evaluation of parallel manipulators: A study on planar parallel manipulators," in *Proc. 7th World Congr. Intell. Control Autom.*, Jun. 2008, pp. 353–357.
- [23] J. Shim, S. Song, D. Kwon, and H. Cho, "Kinematic feature analysis of a 6-degree-of-freedom in-parallel manipulator for micro-positioning surgical," in *Proc. IEEE/RSJ Int. Conf. Intell. Robots Syst.*, Sep. 1997, vol. 3, pp. 1617–1623.
- [24] J. Burgner *et al.*, "A telerobotic system for transnasal surgery," *IEEE/ASME Trans. Mechatronics*, vol. 19, no. 3, pp. 996–1006, Jun. 2014.
- [25] H. Hu, P. Wang, B. Zhao, M. Li, and L. Sun, "Design of a novel snake-like robotic colonoscope," in *Proc. IEEE Int. Conf. Robot. Biomimetics*, Dec. 2009, pp. 1957–1961.
- [26] A. Bajo, R. E. Goldman, L. Wang, D. Fowler, and N. Simaan, "Integration and preliminary evaluation of an insertable robotic effectors platform for single port access surgery," in *Proc. IEEE Int. Conf. Robot. Autom.*, May 2012, pp. 3381–3387.
- [27] P. Qi, H. Liu, L. Seneviratne, and K. Althoefer, "Towards kinematic modeling of a multi-dof tendon driven robotic catheter," in *Proc. 36th Annu. Int. Conf. IEEE Eng. Med. Biol. Soc.*, Aug. 2014, pp. 3009–3012.
- [28] C. A. Seneci *et al.*, "Design and evaluation of a novel flexible robot for transluminal and endoluminal surgery," in *Proc. IEEE/RSJ Int. Conf. Intell. Robots Syst.*, Sep. 2014, pp. 1314–1321.
- [29] J. Granna and J. Burgner, "Characterizing the workspace of concentric tube continuum robots," in *Proc. 41st Int. Symp. Robot.*, Jun. 2014, pp. 1–7.
- [30] I. Gravagne *et al.*, "Manipulability, force, and compliance analysis for planar continuum manipulators," *IEEE Trans. Robot. Autom.*, vol. 18, no. 3, pp. 263–273, Jun. 2002.
- [31] K. Xu, M. Fu, and J. Zhao, "An experimental kinesthetic comparison between continuum manipulators with structural variations," in *Proc. IEEE Int. Conf. Robot. Autom.*, 2014, pp. 3258–3264.
- [32] T. Yoshikawa, *Foundations of Robotics: Analysis and Control*. Cambridge, MA, USA: MIT Press, 1990.
- [33] K. Xu and N. Simaan, "An investigation of the intrinsic force sensing capabilities of continuum robots," *IEEE Trans. Robot.*, vol. 24, no. 3, pp. 576–587, Jun. 2008.
- [34] K. Xu and N. Simaan, "Intrinsic wrench estimation and its performance index for multisegment continuum robots," *IEEE Trans. Robot.*, vol. 26, no. 3, pp. 555–561, Jun. 2010.
- [35] A. Bajo and N. Simaan, "Finding lost wrenches: Using continuum robots for contact detection and estimation of contact location," in *Proc. IEEE Int. Conf. Robot. Autom.*, 2010, pp. 3666–3673.
- [36] D. C. Rucker and R. J. Webster, III, "Deflection-based force sensing for continuum robots: A probabilistic approach," in *Proc. IEEE/RSJ Int. Conf. Intell. Robots Syst.*, 2011, pp. 3764–3769.
- [37] J. Back, T. Manwell, R. Karim, K. Rhode, K. Althoefer, and H. Liu, "Catheter contact force estimation from shape detection using a real-time Cosserat rod model," in *Proc. IEEE/RSJ Int. Conf. Intell. Robots Syst.*, 2015, pp. 2037–2042.
- [38] M. Khoshnam, A. Skanes, and R. V. Patel, "Modeling and estimation of tip contact force for steerable ablation catheters," *IEEE Trans. Biomed. Eng.*, vol. 62, no. 5, pp. 1404–1415, May 2015.
- [39] C. E. Bryson and D. C. Rucker, "Toward parallel continuum manipulators," in *Proc. IEEE Int. Conf. Robot. Autom.*, 2014, pp. 778–785.
- [40] J. Till, C. E. Bryson, S. Chung, A. Orekhov, and D. C. Rucker, "Efficient computation of multiple coupled Cosserat rod models for real-time simulation and control of parallel continuum manipulators," in *Proc. IEEE Int. Conf. Robot. Autom.*, 2015, pp. 5067–5074.
- [41] J. Till and D. C. Rucker, "Elastic stability of Cosserat rods and parallel continuum robots," *IEEE Trans. Robot.*, vol. 33, no. 3, pp. 718–733, Jun. 2017.
- [42] D. C. Rucker and R. Webster, "Computing Jacobians and compliance matrices for externally loaded continuum robots," in *Proc. IEEE Int. Conf. Robot. Autom.*, 2011, pp. 945–950.
- [43] S. S. Antman and S. Antman, *Nonlinear Problems of Elasticity*, vol. 107. New York, NY, USA: Springer, 2005.
- [44] R. M. Murray, Z. Li, and S. S. Sastry, *A Mathematical Introduction to Robotic Manipulation*. Boca Raton, FL, USA: CRC Press, 1994.
- [45] P. L. Anderson, A. W. Mahoney, and R. J. Webster, "Continuum reconfigurable parallel robots for surgery: Shape sensing and state estimation with uncertainty," *IEEE Robot. Autom. Lett.*, vol. 2, no. 3, pp. 1617–1624, Jul. 2017. [Online]. Available: <http://ieeexplore.ieee.org/document/7872425/>
- [46] A. W. Mahoney, P. L. Anderson, P. J. Swaney, F. Maldonado, and R. J. Webster, "Reconfigurable parallel continuum robots for incisionless surgery," in *Proc. IEEE/RSJ Int. Conf. Intell. Robots Syst.*, Oct. 2016, pp. 4330–4336. [Online]. Available: <http://ieeexplore.ieee.org/document/7759637/>
- [47] Y. Zhu, J. Yang, H. Jin, X. Zang, and J. Zhao, "Design and evaluation of a parallel-series elastic actuator for lower limb exoskeletons," in *Proc. IEEE Int. Conf. Robot. Autom.*, May 2014, pp. 1335–1340.
- [48] M. Grimmer, M. Eslamy, S. Glied, and A. Seyfarth, "A comparison of parallel- and series elastic elements in an actuator for mimicking human ankle joint in walking and running," in *Proc. IEEE Int. Conf. Robot. Autom.*, May 2012, pp. 2463–2470.
- [49] W. Curtis, J. D. Logan, and W. Parker, "Dimensional analysis and the Pi theorem," *Linear Algebra Appl.*, vol. 47, pp. 117–126, 1982.
- [50] S. Thrun, W. Burgard, and D. Fox, *Probabilistic Robotics*. Cambridge, MA, USA: MIT Press, 2005.
- [51] 2016. [Online]. Available: <http://www.omega.com/das/pdf/OM-DAQ-USB-2400.pdf>



Caroline B. Black (S'13) received the B.S. degrees in mechanical engineering and nursing from University of Alabama in Huntsville, Huntsville, AL, USA, in 2013 and the Ph.D. degree in biomedical engineering from The University of Tennessee, Knoxville, TN, USA, in 2017.

She is currently teaching with University of Alabama in Huntsville. Her research interests include medical technology, robotics, and STEM outreach.



John Till (S'14) received the B.S. degree in mechanical engineering from Tennessee Technological University, Cookeville, TN, USA, in 2014. He is currently working toward the Ph.D. degree in mechanical engineering with The University of Tennessee, Knoxville, TN, as a Graduate Research Assistant in the Robotics, Engineering, and Continuum Mechanics in Healthcare Laboratory.

His research interests include continuum robotics, real-time computation, and medical devices.



D. Caleb Rucker (M'13) received the B.S. degrees in engineering mechanics and mathematics from Lipscomb University, Nashville, TN, USA, in 2006 and the Ph.D. degree in mechanical engineering from Vanderbilt University, Nashville, in 2010.

From 2011 to 2013, he was a Postdoctoral Fellow with the Department of Biomedical Engineering, Vanderbilt University, before joining The University of Tennessee, Knoxville, TN, in 2013, as an Assistant Professor of mechanical engineering, where he directs the Robotics, Engineering, and Continuum Mechanics in Healthcare Laboratory.